Results in Materials 20 (2023) 100456

Contents lists available at ScienceDirect

Results in Materials

journal homepage: www.sciencedirect.com/journal/results-in-materials

Numerical modelling of DMLS Ti6Al4V(ELI) polygon structures

M.I. Chibinyani [a,*], T.C. Dzogbewu [a], M. Maringa [a], A.M. Muiruri [a,b]

[a] Department of Mechanical and Mechatronics Engineering, Central University of Technology, Free State, South Africa
[b] Department of Mechanical and Manufacturing Engineering, Southern Eastern University of Kenya, Kitui, Kenya

ARTICLE INFO

Keywords:
Lattice structures
Tessellation
Polygon structures
Analytical modelling
Numerical modelling

ABSTRACT

Numerical modelling is particularly advantageous for analysing structures with complex behaviour. It is used to predict the mechanical properties of structures. Analytical modelling, on the contrary, has limited capacity for predicting the behaviour, particularly of structures, because it is based on mathematical equations that do not always exactly represent the geometry of the model. In such cases, numerical modelling is used for predicting structural bending, axial deformation, and buckling behaviour. This study documents numerical modelling of different types of polygon structures. To reduce computation costs, planar and extruded Ti6Al4V(ELI) hexagonal shell structures were used to predict stresses in the out-of-plane and in-plane directions. This was followed by numerical modelling of different types of planar polygon structures to predict their load-bearing capacity and stiffness. Thereafter, the hexagonal polygon was subjected to out-of-plane and in-plane uniaxial compression loads. This was done to compare the bending and buckling behaviour of finite element (FE) models to analytical models. The numerical and analytical results were then compared to determine how the ratio (t/L) of the wall thickness (t) and length of the polygon members (L) influenced the effective stiffness of the hexagonal polygon. The triangular polygon was seen to have the greatest load-bearing capacity and stiffness of all polygons that were modelled. The hexagonal model was observed to generate deformations due to compression, similar to those reported in literature. The critical buckling loads for the analytical honeycomb (HC) models were found to be below the yield stress for (1-, 1.125-, and 1.25-mm wall thicknesses) and above the yield stress for all FE HC models, respectively. The effective stiffness of the HC models were observed to increase with the increasing (t/L) ratio, for both the numerical and analytical models.

1. Introduction

The current work is part of broad research on additive manufacturing (AM) and qualification of Ti6Al4V(ELI-Extra low interstitial) for applications in the medical and aerospace industries, at the Centre for Rapid Prototyping and Manufacturing (CRPM) of the Central University of Technology - Free State, in South Africa. The Ti6Al4V alloy has good mechanical properties, including high strength [1], high fracture toughness [2,3], significant resistance to both corrosions [4] and wear degradation at normal and elevated temperatures [5,6], good biocompatibility [7,8], and the physical property of low density [1–4,6–8]. Fabricating Ti6Al4V into lattice structures, particularly polygonal structures, provides a compelling set of advantages [1,4]. These include reduced weight, improved mechanical properties, capacity to customize, biocompatibility, improved thermal management, and compatibility with cutting-edge manufacturing methods such as AM [1,4,6,7]. Lattice parts fabricated from Ti6Al4V are advantageous for use in challenging applications spanning numerous engineering sectors [1–3,6–8].

Lattice structures such as polygon structures have good load-bearing capacity based on how efficiently they are distributed in a design space [9]. These structures are made of porous materials with topologies formed from combining periodic unit cells or a unit cell [9,10]. Lattice structures are achieved through tessellation, which is a process of packing unit cells together in a repeating pattern with no gaps or overlaps using mathematical functions [10]. Triangles, squares, circles, and hexagons are some other polygonal cell types used to create lattice structures [11]. Lattice structures yield good mechanical properties, with less usage of material. Their mechanical properties depend on the shape of the cells, aspect ratio of members, connectivity of cell edges, their relative density, size of cells, and structural properties of the parent material [12].

* Corresponding author.
E-mail addresses: chibinyanimunashe@gmail.com (M.I. Chibinyani), tdzogbewu@cut.ac.za (T.C. Dzogbewu), mmaringa@cut.ac.za (M. Maringa), amuiruri@seku.ac.ke (A.M. Muiruri).

https://doi.org/10.1016/j.rinma.2023.100456
Received 12 July 2023; Received in revised form 8 September 2023; Accepted 11 September 2023
Available online 12 September 2023
2590-048X/© 2023 The Authors. Published by Elsevier B.V. This is an open access article under the CC BY-NC-ND license (http://creativecommons.org/licenses/by-nc-nd/4.0/).

Applying tessellation assists in production of structures with different cell topologies. In order to compare the efficiency of filling of a space with a prescribed area by four different polygons, including triangular, square, hexagonal, and circular polygons, the four are related as shown in Fig. 1. It is clear the circle circumscribes the other three, where the vertices of the polygons are defined by their points of intersection with the circular polygon.

It is illustrated in Fig. 2, how planar structures within the same space can be created from tessellating different polygons in a plane, such as triangles, squares, circles, and hexagons. The extent of use of the provided space determines the efficiency of utilising the design space for structures formed by the tessellation of polygons [13,14]. The efficient use of the design space leads to structures with good mechanical properties. Through tessellation, the mechanical properties of structures can be determined with respect to the deduced relationships between the connecting edges and vertices of cells [12]. Therefore, structures that are formed from different types of arrangement of polygons will have different mechanical properties [13].

Fig. 2 demonstrates how different polygons that are tessellated on the same design space produce varied numbers of polygons, area-coverage, and material use with reference to the same wall thickness. The squared, triangular, hexagonal, and circular polygons are seen in this figure to have area-coverages of, 100%, 99.78%, 93.93%, and 78.54%, respectively, ignoring the very small incomplete polygon shapes in Figure (2a and 2d). For the same polygons, in the same order, the percentage values for the amount of material used, referenced to the area of the full design space, are, 15.28%, 20.81%, 10.32%, and 7.85%, respectively. The amount of material used for each polygon type was determined by considering the wall thickness of the polygon structure as 1 mm.

When tessellated in a design space, the square polygon is clearly the preferred shape in terms of area-coverage. This is due to the fact that it has the highest area-coverage of the design space. The circular polygon is likely to have the lowest cost of production, as it requires the least amount of material. Yet, when compared to the other polygons, the hexagonal polygon is the most preferrable since it combines an area-coverage that is slightly less than the polygon with the highest area-coverage, and material-usage that is significantly less than the square polygon.

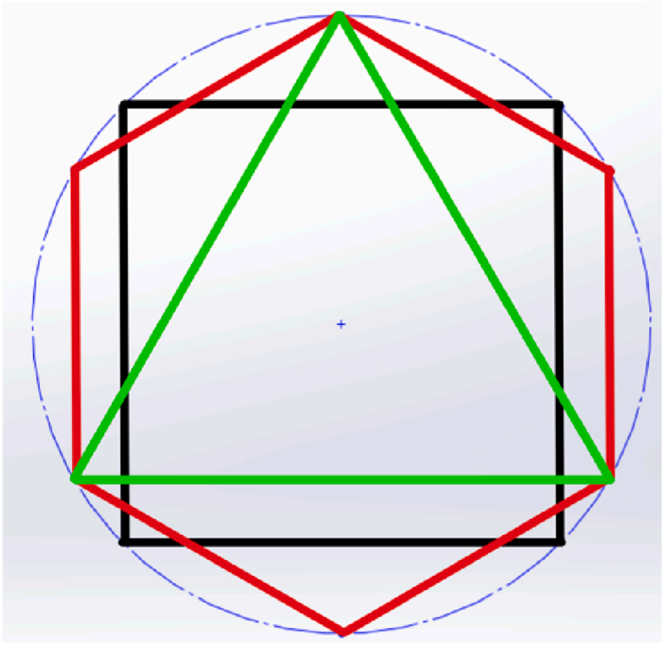


Fig. 1. The relationship between four different types of cell polygons within the same design space.

Lattice structures are strong and stiff when load is applied in the in-plane directions but have low stiffness when loaded out-of-plane and are therefore, expected to fail first, under out-of-plane loads. Out-of-plane loads causes bending deflection in a structural frame. In-plane loading causes members, to undergo axial compression and/or buckling behaviour [14]. Applying the same magnitude of load in the out-of-plane and in-plane directions of a structural frame results in higher stresses for bending loads compared to direct and buckling loads [15]. It is important to note that compression stiffness in lattice structures is influenced by direct deformation and/or buckling behavior, with either becoming critical depending on the values of the geometrical parameters defining the cross-section and length [12,14,16]. According to Gibson and Ashby [17], the orientation of a planar lattice structure relative to the applied loads, influences its mechanical properties. As a result, its use is limited by the direction of the applied loads and orientation of the structure [16].

Lattice structures are highly stressed at the vertices and are thus prone to failure in these areas even at low applied loads. The high stresses seen in such areas are a result of sharp changes of geometry that occur at the vertices [18]. According to a number of studies, the size of the angle at the vertices can influence the maximum value of stress concentration at the vertex regions [13,15,17,18]. High magnitudes of stress at the vertices, result from using geometries with smaller angles at the vertices [15–18]. The research of Helou & Kara [16], and Gibson & Ashby [17] compared and ranked the triangular, squared and/or rectangular, circular, and hexagonal polygon structures in terms of efficiency. It was observed in these works that the tessellation of all of these cells results in lattice structures with good mechanical and physical properties. The hexagonal and circular structures were found by the same authors to have much lower stiffness than the other aforementioned polygon structures. Except for the circular structure, which has tangential connectivity of the polygons in a design space, the other three polygon structures have complete connectivity of their adjacent sides. Moreover, the hexagonal structure has larger or obtuse angles at the vertices (θ=120°) which reduces the abrupt or sharp changes of geometry at the vertices compared to the acute and 90° angles created at the vertices of triangular (θ=60°) and squared (θ=90°) structures, respectively. The larger angles at the vertices of the hexagonal structure reduce the degree of stress concentration experienced at these regions compared to those of the other three polygon structures. In comparison, structures built with circular polygons have greater magnitudes of stress. This is because the sharp changes of geometry observed at the points of intersection of circular polygons experience high degrees of stress concentration. These areas of high stress concentration are crucial in the resulting failure of respective polygon structures [17,18]. A circular polygon's geometry is rigid on its own, but the corners generated by joining the polygons are sharp, leading to higher concentrations of stresses at these regions. The structures thus formed experience localized deformation due to high concentration of stresses in the regions near the corners.

The review in this section indicates that the triangular polygon design is the most likely to lead to the highest stress concentration, followed by the squared and/or rectangular polygon and the two have higher values of stiffness than the circular and hexagonal polygons. Therefore, hexagonal, and circular structures are better for load carrying capacity and absorption of energy. Triangular cells are more resilient to bending and deform mostly as a result of axial and/or buckling behaviour. This is due to the fact that the triangular shape evenly spreads stresses over all its three sides. Triangular cells are particularly well-suited to withstand axial loads and reducing lateral movement. However, it is not clear from the foregoing review, which one of these latter two types of polygons is more likely to withstand higher loads than the other, a fact that is addressed further on in this paper.

In the past three decades, efforts to improve absorptions of strain energy in automobile and aircraft lightweight structures exposed to

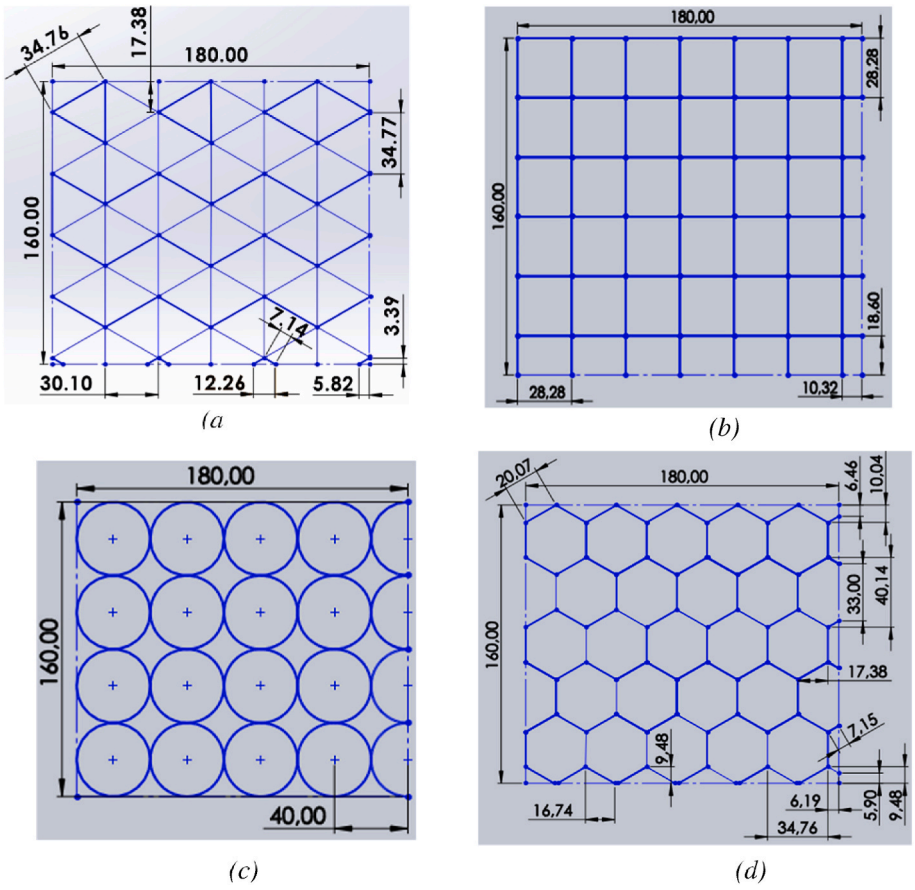


Fig. 2. Tessellated planar structures using (a) triangular, (b) squared, (c) circular and (d) hexagonal cells.

crushing loads have intensified. This has promoted the manufacturing of lightweight cellular structures with good load bearing capacities [19]. To manufacture such structures, AM methods such as direct metal laser sintering (DMLS), a subset of laser powder bed fusion (LPBF) can be used. The DMLS method uses metal powders such as Ti6Al4V (ELI) to manufacture cellular structures. The mechanical behaviour of such structures can be predicted primarily using analytical models, but better and faster insights can arise from using numerical models [20]. Analytical models are limited by their theoretical formulation, require several modelling assumptions to be made, and often differ from the ideal conditions. The numerical models on the other hand offer a quick way of determining whether ideas are physically implementable or not [20–22].

Numerical simulation can be used to qualify the behaviour of lightweight polygon structures in biomedical, aerospace, and automotive industries [20,21]. Polygon structures are made up of thin-walled plates, which have delicate structural stability, and are liable to fail at low applied stress loads [23]. The structures manifest a crushing behaviour, which is dependent on the parameters of cell shape (the internal angle, θ, of the polygon cells) and wall thickness (t) [24]. To reduce failure of the structures, careful analysis, and optimisation of the parameters θ and t is required. In theoretical analysis, the analytical model tends to overestimate these parameters unlike the numerical models [21]. According to Goldmann et al. [22], finite element models of honeycomb (HC) structures are more accurate than an analytical models. This contrasts with the results obtained by Malek and Gibson [23]. They found a close relationship between the analytical and finite element models. However, they only looked at a single cell without considering the effect of the boundaries. From what was recorded by Gibson [24] and in contrast by Malek and Gibson [23], the theoretical model could slightly overestimate structural stiffness. This difference, however, is small being of the order of 0.1%. The difference in the relative effective stiffness obtained from the analytical and numerical models of Goldmann et al. [22] is slightly greater at approximately 0.8%. This could be explained by the fact that the analytical model ignores deformation at the nodes. Their numerical simulation in this work revealed that the highest stresses act at the nodes, affecting their deformation, which emphasizes the significance of the observed difference of stiffness. The authors validated their results further by demonstrating that failure during experiments was mostly observed at the nodes.

Several analytical modelling studies have been conducted to predict the effective stiffness of a regular hexagonal structure based on optimisation of its geometric parameters. Gibson et al. [17,25] developed analytical equations for the effective stiffness based on a cell wall bending model. This is a beam model that is fixed at one end and transversely loaded at the other end. Warren and Kraynik [26] introduced a new model based on the cell wall bending and stretching to predict the effective stiffness of a periodic cellular structure. Gibson and Ashby [17] later proposed preferred models for predicting effective stiffness. These models considered bending, stretching, and shearing of the cell walls. In contrast, a limited number of finite element (FE) methods and advanced computational technique studies have been conducted to predict the effective stiffness of polygon structures [27–30]. The limited studies based on HC structures were loaded to the maximum elastic stress. Through numerical modelling, better insights, more exact and quicker predictions of mechanical properties for structures with varying geometric parameters are achievable [11,12].

At the outset of this study, four polygons including the triangular, squared, circular, and hexagonal geometries were numerically modelled to compare and rank them in terms of efficiency. This was followed by analysis to provide a direct comparison between the numerical results of the best of these four polygon structures and its theoretical behaviour.

The theoretical behaviour was predicted by adopting analytical models already in literature and using them to generate results for a Ti6Al4V (ELI) structure of the best polygon, with different values of the parameter *t*. The influence of parameter *t* on the effective stiffness of the structures was investigated under simple compression. Numerical modelling was then carried out with the same variables adopted for the analytical models. The predictions of the analytical models were then compared with those from numerical modelling. A further numerical test was carried out to investigate the influence of parameter *t* on the buckling behaviour of the structure for the best polygon.

2. Materials and methods

2.1. Polygon part design

Two different geometry designs, a planar and an extruded hexagonal polygon shell, generated in SolidWorks (2020), were used in this study. The geometries were generated using primary parameters such as the outer cell shape ($\theta = 240°$) and length (L= 20 mm), as shown in Fig. 3 (a). The value of the parameter *t* that was allocated to the planar hexagonal shell was 1 mm, whereas the extruded hexagonal shell had *t* values ranging from (1, 1.125, 1.25, 1.375, 1.5, 1.625 and 1.75) mm. These geometries were then imported into ABAQUS/CAE (version 2020) for their analysis with applied loads.

SolidWorks was additionally used to develop planar structures based on three other geometries, including triangular, squared, and circular polygons, with t= 1 mm, as shown in Fig. 4, which were also analysed numerically, in ABAQUS/CAE.

2.2. Analytical modelling

The effective density model used to predict the analytical behaviour of the selected polygon structures in this study was the same one used by Gibson and Ashby [17], and is expressed as shown in Equation (1):

$$\frac{\rho^*}{\rho_s} = \frac{2}{\sqrt{3}}\frac{t}{L} \tag{1}$$

where, ρ^* and ρ_s are the densities of the specific structure and solid material, respectively.

Gibson and Ashby [17] modelled the stiffness of regular HC structures in compression tests with regard to the effective stiffness E^{eff}. This effective stiffness is an estimated theoretical modulus of a homogeneous material that has the same stress-strain behaviour as the cellular structure. Their model estimated bending and axial behaviour of HC structures according to the Euler-Bernoulli beam theory, while neglecting the deformations occurring within the nodes [16,17,23]. Taking into consideration deflection due to compression, bending and axial behaviour, the effective stiffness of the regular hexagonal structure was, therefore, estimated as follows:

$$\frac{E^{eff}}{E_s} = \frac{E_x^{eff}}{E_s} = \frac{E_y^{eff}}{E_s} = \frac{4}{\sqrt{3}}\left(\frac{t}{L}\right)^3 \tag{2}$$

where the symbols, E_x^{eff} and E_y^{eff} represent the effective stiffness in the *x*- and *y*-axis directions, respectively. The symbol E_s stands for the elastic modulus of the solid material. The Gibson and Ashby model presented in Equation (2) assumed stiffness can be varied by changing parameters such as the wall thickness, which is known to be related to the effective stiffness. Throughout this study, the *t/L* ratio was varied from 0.05 to 0.0875 at 0.00625 intervals, while the length of the cell wall's mid-plane was held constant. The resulting ratios of effective stiffness along the *x*- and *y*-axis to the elastic modulus of the solid material were calculated and recorded as shown in Table 1.

The analytical predictions in Table 1 were then compared to the numerical results obtained in the present work in the numerical modelling section. Another investigation was carried out with regard to elastic buckling behaviour of the selected polygon structures. The analytical model adopted for this investigation was the same one developed by Gibson and Ashby [17,25]. A critical Euler buckling load was determined in this investigation for its first or primary buckling shape that occurs when the structure is loaded along the z-axes. Gibson and Ashby's work estimated the magnitudes of crucial buckling stress (the stress corresponding to the critical buckling load) for linear buckling to occur using the following equation [17]:

$$\left(\sigma_{el}^c\right)_z = 5.2\,E_s\left(\frac{t}{L}\right)^3 \tag{3}$$

where, $(\sigma_{el}^c)_z$ is the crucial buckling stress that occurs for loading in the z-direction. It is highlighted in Gibson et al. [25] that linear buckling for loading in the x- and y-directions in a similar set up shown in Fig. 3, are regarded as being trivial because the structural frames modelled experience critical bending loads before critical buckling loads in these directions. Therefore, linear buckling for loading in these directions can be neglected, unlike in the z-direction.

2.3. Finite element (FE) modelling

Numerical modelling of Ti6Al4V(ELI) polygon structures was carried out using ABAQUS/CAE (Version 2020). Regular polygon structures, which were generated using different cell types and wall thickness, were simulated, respectively. The values of the properties of the Ti6Al4V(ELI)

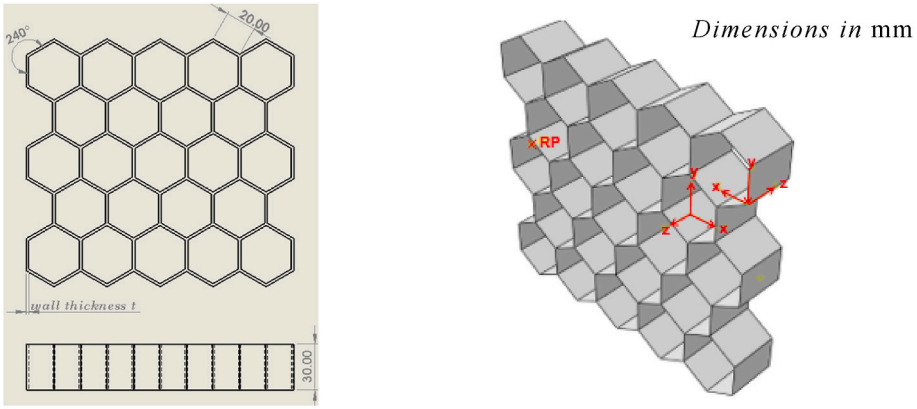


Fig. 3. Typical (a) planar HC shell (b) extruded HC shell structures.

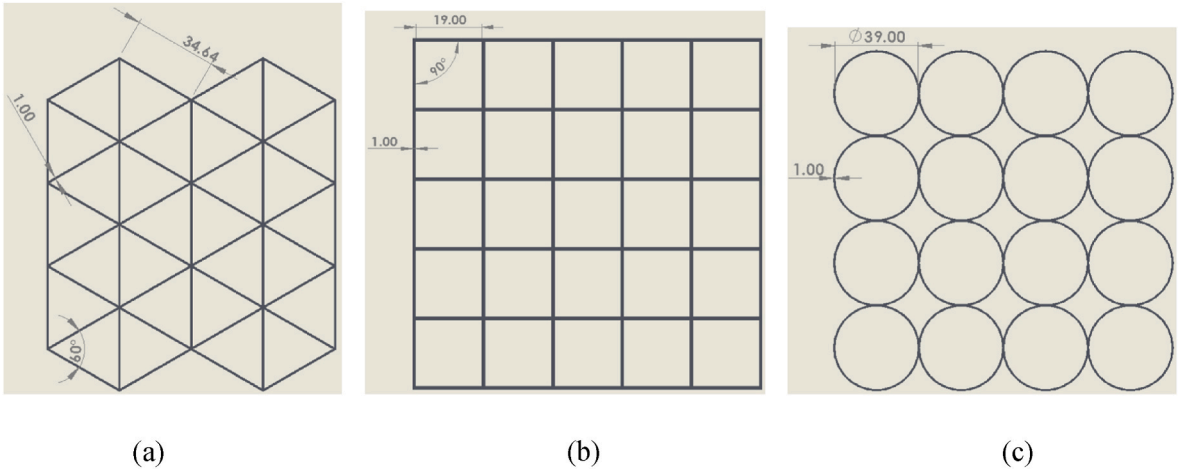


Fig. 4. Typical planar (a) triangular, (b) squared, and (c) circular polygon shell structures.

Table 1
Ratios of effective elastic modulus to the elastic modulus of the solid material.

t/L	E^{eff}/E_s
0.05	0.000289
0.05625	0.00041
0.0625	0.000564
0.06875	0.000753
0.075	0.000974
0.08125	0.00124
0.0875	0.00155

material used in these polygon models are listed in Table 2 [31]. The Ti6Al4V (ELI) alloy is an (α+β) type of alloy, which has four basic microstructures. These include lamellar, equiaxed, martensite and bimodal microstructures [32]. The phase fractions of these microstructures of titanium alloys can be varied by various heat-treatment processes [31]. The lamellar and equiaxed microstructures are achieved through slow cooling and recrystallisation processes, respectively. A pure lamellar microstructure is attained by slowly cooling from the β phase field. Rapid cooling, however, transforms the microstructure to one that features a fine needle-like martensitic microstructure [8]. To achieve the equiaxed microstructure, the alloy must first be highly deformed in the α+β phase field to introduce acceptable cold work into the material. After subsequent solution heat-treatment at temperatures in the α+β phase field, an equiaxed microstructure that has recrystallized is formed [31].

In thermomechanical treatment process, there could be an occurrence of a central point, β-transus temperature, which separates the β phase field from the α+β phase field [8,31,32]. With reference to this central point, the last type of allotropic transformation, bimodal microstructure is achieved when a solution heat treatment is employed just below the β-transus temperature. The bimodal microstructure consists partly of equiaxed (primary) α phase in a lamellar α+β matrix. This microstructure is therefore a result of combining lamellar and equiaxed microstructure [8]. Equiaxed microstructures have high ductility and fatigue strength and are preferred for superplastic deformation, whereas lamellar microstructures have high fracture toughness and superior resistance to creep and fatigue crack growth [32]. Bimodal microstructures have a well-balanced property profile because they combine the advantages of lamellar and equiaxed structures [8]. The bimodal microstructure is, therefore, suited for the polygon structures since the mechanical properties of a material is dependent on its microstructure. The mechanical properties of Ti6Al4V(ELI) with bimodal microstructure chosen for this study is presented in Table 2.

Table 2
Material properties of Ti6Al4V(ELI) used in FE modelling of polygonal structures [31].

Material property	Mass Density (ρ)	Young's Modulus (E)	Poisson's Ratio (ν)	Yield Stress (σ_{ys})
Magnitude	4430 kg/m^3	113.8 GPa	0.342	790 MPa

For simple and faster finite element analysis (FEA), the stress distribution in the xy-plane and out-of-plane (z) direction of a HC structure was determined at the onset using planar and extruded hexagonal shell geometry, respectively. This was done to determine how representative the results of the planar model were of the HC structure, as the former is simpler and faster to run, for later use in comparing the behaviour of different polygon structures under load. In this analysis, a mesh with S8R type of shell elements was generated on a planar and extruded hexagonal shell geometry with 1 mm thick walls. These second-order shell elements have a significant advantage of computation speed and employ simplified methods of calculating strain and hourglass control. The mesh size on the two geometries was then varied within the range of 0.2–1 mm. This was done such that the large mesh size of 1 mm was located in the middle regions of the wall members and reduced moving towards the edges and vertices (0.2 mm), as shown in Fig. 5. This was done in order to accurately capture results at the vertices and edges, which are known to be areas of high-stress concentration. This was followed by simulation under a simple uniaxial compression load of 2000 N applied to each one of the two model geometries as shown in Fig. 6.

The compression load was applied using rigid plates on opposing ends of the model. The interfaces between the two rigid plates and each

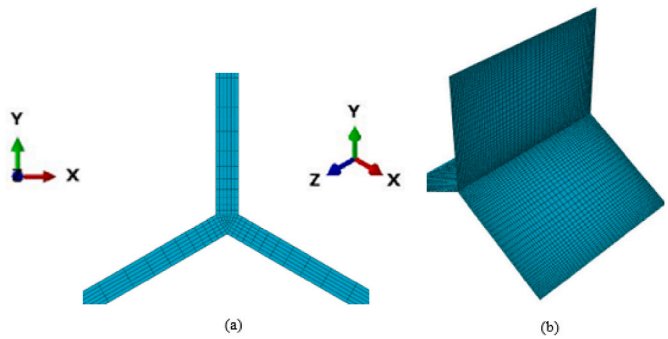


Fig. 5. Models of (a) planar hexagonal shell walls and (b) extruded hexagonal shell walls, generated using different element sizes.

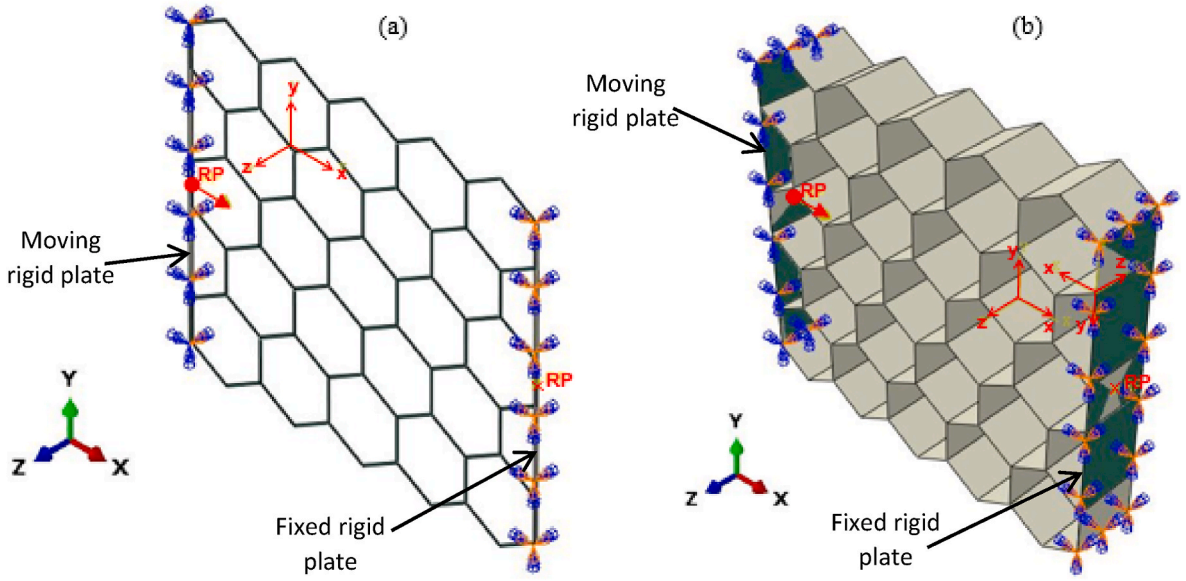


Fig. 6. Typical, (a) planar hexagonal shell and (b) extruded hexagonal shell, models with boundary conditions.

one of the two models were assigned a frictionless contact and the normal interaction property modelled as a hard contact to prevent the model penetrating the rigid surface. One rigid plate for the two models was assigned fixed constraint and a load applied on the other, as shown in Fig. 6. The latter rigid plate was constrained and only allowed to move in the direction of the load.

Simulation tests based on the boundary conditions shown in Fig. 6a and b were used to determine the stress distributions in the xy and z-axis of the HC models, respectively. In these simulation tests, contour plots of stress results were obtained. Unit cells cut off from the central region of the planar and extruded hexagonal or HC, shell models were then used for analysis of the arising stresses as shown in Fig. 8, in the section on results and analysis.

In the ensuing analysis, the planar hexagonal shell model was used to compare and rank triangular, rectangular, circular, and hexagonal planar models for the same load of 2000 N applied along the x- and y-directions. The obtained numerical results were also compared to the theoretical results. Because the hexagonal or HC model is the most extensively researched polygon cell type, it was used in all ensuing polygonal model investigations to allow for a more accurate comparison of results and literature. This cell type was simulated as an extruded HC shell model with different wall thicknesses for maximum elastic loads, in the x- and y-direction, and the arising numerical results compared to the analytical results in literature.

The HC geometrical models were generated using an extruded shell, which was then discretised into elements. The crushing behaviour of the analysed structure subjected to a simple uniaxial compression load for linear-elastic behaviour was then investigated. This was carried out to predict the elastic bending behaviour of the structure and compare its behaviour with the one predicted from analytical models. Thereafter, the effect of the ratio of thickness to length (t/L) on the effective stiffness for both analytical and numerical results was compared. The effective stiffness was obtained by first determining the maximum direct stresses and then calculating the corresponding strains using the obtained magnitudes of deformation in the FE analysis. The ratio of these two values gave rise to a calculated value of the effective stiffness, which was then divided by the stiffness of the material (E_s) to obtain the stiffness ratio. The value of effective stiffness (E^{eff}) was predicted in the x- or y-directions of the HC model for maximum elastic bending using the following expressions:

$$E_x^{eff} = \frac{\sigma_x}{\varepsilon_x}, E_y^{eff} = \frac{\sigma_y}{\varepsilon_y} \quad (4)$$

where, σ_x and σ_y are the maximum direct stresses in the x- and y-axes, respectively. The symbols ε_x and ε_y are the maximum direct strains in the x- and y-axes, respectively. Numerical analysis was also carried out in this study to predict linear elastic buckling for loading in the z-direction and the results were compared to the theoretical behaviour of the HC structure. The bottom edges of the HC model were fixed in the x, y, and z axes, with no rotations allowed. This meant that the structure could flex and bend along these edges but not leave the bottom's surface when loaded. The top edges and vertices were then assigned equivalent equations to determine the loading constraints of the HC model, which were allocated to specific parts of the structure in pre-defined sets. One set was assigned to the top-driven edges and the other to the top-driving vertex, as shown in Fig. 7(b). A 1000 N load was then applied uniaxially to the top-driving vertices in order to simulate buckling, which same load was felt uniaxially by all of the top driven edges in the z-direction. Fig. 7 shows two additional loading and boundary conditions that were investigated for loading in the y- and z-direction of the extruded hexagonal shell model.

3. Results and discussion

3.1. Comparative analysis of planar and extruded FE models

The stresses in the planar and extruded hexagonal shell models were both found to be highest at the vertices, as shown in Fig. 8(a) and b, respectively. The planar hexagonal shell model in Fig. 8(a) is a plane strain problem. This is because load is applied in a xy-plane of the extruded hexagonal shell model, and the thickness of the shell in the out-of-plane axis (z) is comparatively much higher. This implies that the effect of the applied load along the z-axis can be ignored, and the three-dimensional problem represented by a planar problem [33]. The planar hexagonal shell model was observed to have high stresses on the inner vertices of its inclined members, caused by both direct compressive and bending loads. These stresses give rise to large elastic deformations at the vertices. The Poisson's ratio of the material also leads to the development of small transverse elastic strains in the regions. Similarly, the contour plot for stresses on the extruded hexagonal shell model in Fig. 8 (b) shows the highest stresses to occur on the vertices of the inclined

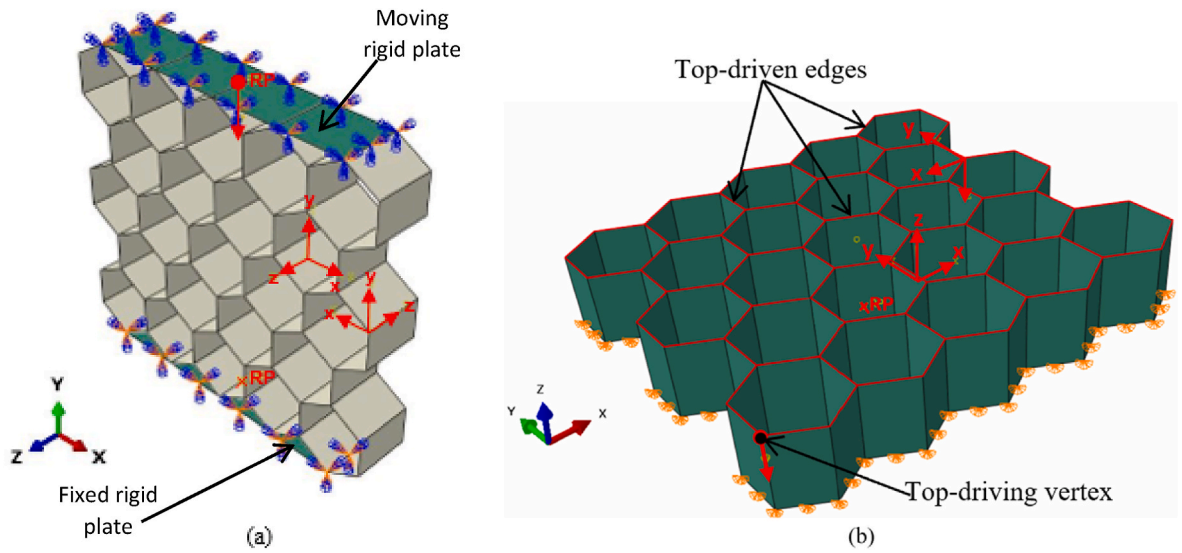


Fig. 7. Loading, fixed and pinned boundary conditions used, respectively, in the (a) y-direction, and (b) z-direction, of an extruded HC shell structure.

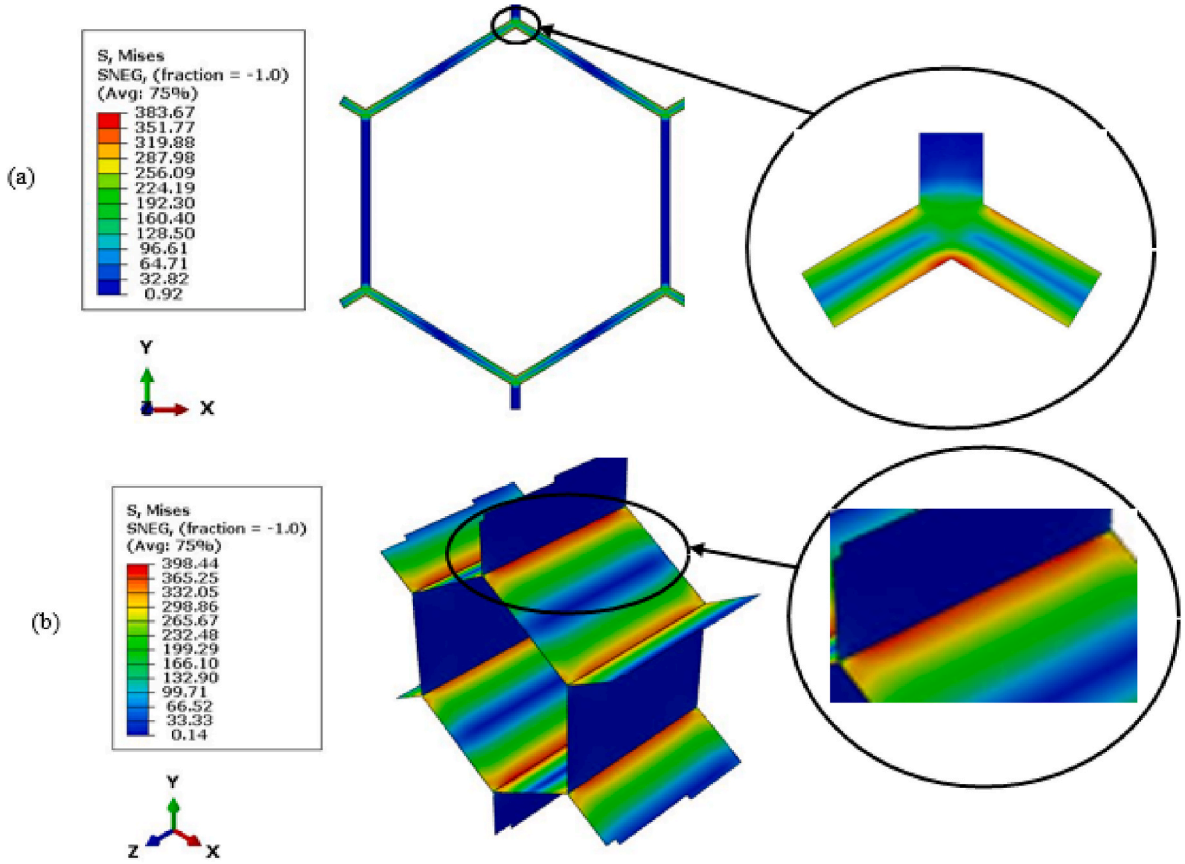


Fig. 8. Typical contour plot of stress obtained on (a) planar hexagonal and (b) extruded hexagonal, shell models.

members. These results are similar to what was observed in Refs. [15–19]. The same distribution of stress was obtained from the analysis of the plane strain problem.

Upon application of a load of 2000 N, the unit hexagon planar and the extruded shell models shown in Fig. 8, show values of maximum von Mises stresses that are almost the same in magnitude being 383.67 and 398.44 MPa, respectively. This small difference of about 3.71% justifies use of the planar model instead of the more complex extruded model in order to save computational time.

When using the extruded HC shell element, a visual problem occurred at the vertices. The visual problem occurred because the faces connecting the vertices of structural members had no congruence. The lack of congruence was observed when the assigned thickness was extruded from the shell as illustrated in Fig. 9. The black arrows shown in Fig. 9, represent the directions of extrusion of the planar shells of the planar geometry.

The difference between the images in Fig. 9 is simply due to the way the wall thickness is depicted in the two cases. Extruding a thickness

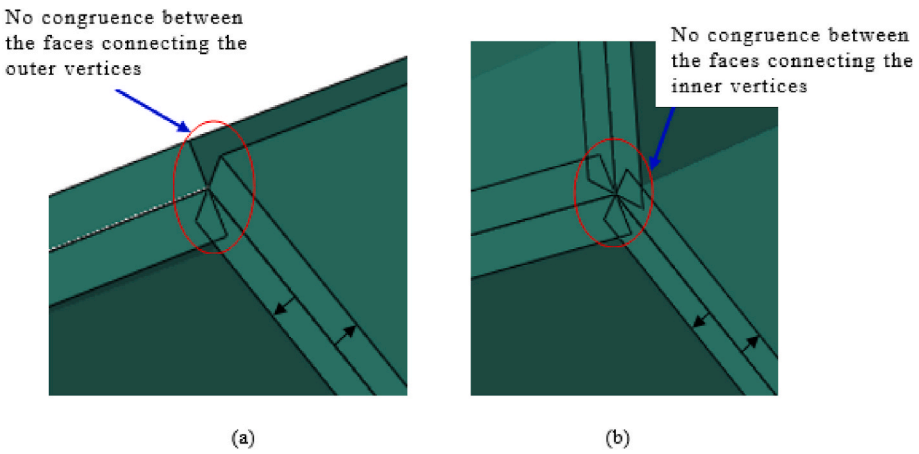


Fig. 9. Typical visual problem of unshared topology at the (a) outer and (b) inner vertices after extruding a thickness from the extruded shell model.

from an extruded shell takes the surface of a shell and extrudes half a wall thickness in either direction. The discrepancy observed at the vertices will occur for any adjacent surfaces meeting at an angle other than 180°, causing some overlap and some gap. This is however only due to the graphical presentation but does not affect the numerical results. The discrepancy referred to at the vertices, however, has limitations when carrying out structural optimisations such as topology and shape optimisation. In recent work by the authors [34], a planar honeycomb model was investigated, and it was concluded that the vertices reduced effective iterations in topology and shape optimisation. Therefore, using geometries with the discrepancy observed at the vertices of extruded hexagonal shell would result in the generation of topologies with no congruence at the vertices, during topology and shape optimisation. This would in turn create difficulties in the normal numerical analysis of the topology and shape optimized structures and is the subject of further research by the authors.

3.1.1. *Preliminary FE results for polygon structures*

Upon applying an out-of-plane load of 2000 N, separately in the x- and y-directions, numerical results were generated for four different planar polygon models with t= 1 mm. These numerical results of stress and deflection are presented in the form of contour plots in Figs. 10–13, respectively. As seen in Fig. 10, the order of increasing maximum stress for different planar polygon models is triangular, squared, hexagonal, and circular, for a load applied in the x-direction. When the load was applied in the y-direction, as shown in Fig. 11, it is observed that the order of preference changed to squared, triangular, circular, and hexagonal models. It is noted that while the values of maximum von Mises stresses for the rectangular and circular models remained the same for loads applied in the x- and y-directions separately, they were higher for loads applied in the y-direction for the triangular and hexagonal models. Loading in the y-direction is therefore, the more critical one for design for the last two polygons.

For loading in the x-direction, it is observed that the triangular and hexagonal models have lower stresses compared to the similar case of loading in the y-direction. This is because the load is applied transversely on the members in the x-direction loading, and at the points of intersection of members in the y-direction loading. The higher stress levels in the second case arise from the fact that loading at the intersection of members occurs in regions of the structure with sharp changes of geometry or apexes. Loading at apex regions of a structure is known to cause high-stress concentration in them [33]. The model of triangular polygons recorded the lowest stresses when loaded in the x-direction. This structure can be argued to have a relatively larger effective cross-sectional area for this type of loading because of the four members carrying the load, in contrast to the models of square and hexagonal polygons, with two members each that are perpendicular and inclined to the applied load, respectively, as shown in Figs. 10 and 11. The circular polygon has the highest x-direction stress (404.183 MPa) and the second highest y-direction stress (404.183 MPa). This is because of the formation of tangential connections between adjacent circular polygons during their tessellation. Furthermore, when moving towards the points of contact or tangential connection, the material that forms the wall thickness of the connected circular polygons decreases, and sharp corners are generated as a result of this type of connection. These points of contact are, therefore, areas of high-stress concentration. For loads applied in the y-direction, the model of square polygons records the lowest stresses, compared to other polygons. It's achieving first position, this time round, is because the model of triangular polygons is now loaded at the apex areas (designated as highly stressed regions) rather than transversely on its members that are connected to members that are inclined to it, for loading in the x-direction. It is deduced from the foregoing discussion that the regions with abrupt changes of geometry also referred to as peak regions, where the load is applied, and the number of members carrying the applied load, determine the load bearing capacity and therefore, stability of polygonal structures. This is consistent with what was reported in Ref. [12].

Table 3 shows a ranking of maximum stresses in the four polygonal structures shown in Figs. 10 and 11.

The data in the preceding table shows the model of triangular polygons to have the lowest and second lowest maximum von Mises stress of all four polygon structures for a load of the same magnitude applied in the x-direction and y-direction, respectively. Clearly, the triangular polygon is the best alternative of the four polygons modelled here.

In Figs. 12 and 13, the circular polygon model is observed to have the largest magnitudes of deflection compared to all other polygon models for loading in both directions. This is similar to what was construed in Ref. [17] and implies that the lattice structures made up of circular polygons are less effective in stiffening structures [35].

Table 4 shows ranking of the deflections for the four different types of polygonal structures.

It is evident from the results presented in Figs. 12 and 13 that the models of triangular and square polygons have the lower and second lowest deflections for loading in both x- and y-directions, respectively. This means that the polygon structures made of the two polygons are stiffer compared to those of circular and hexagonal polygons, which recorded the highest and second highest deflections of all four polygon structures, in both directions, respectively.

From the foregoing work, the triangular polygon records the lowest deflections of all four polygons modelled for a load of the same magnitude and applied in each of the two directions, separately. It also records the lowest maximum von Mises stress for a load of the same magnitude applied in the x-direction and the second lowest maximum

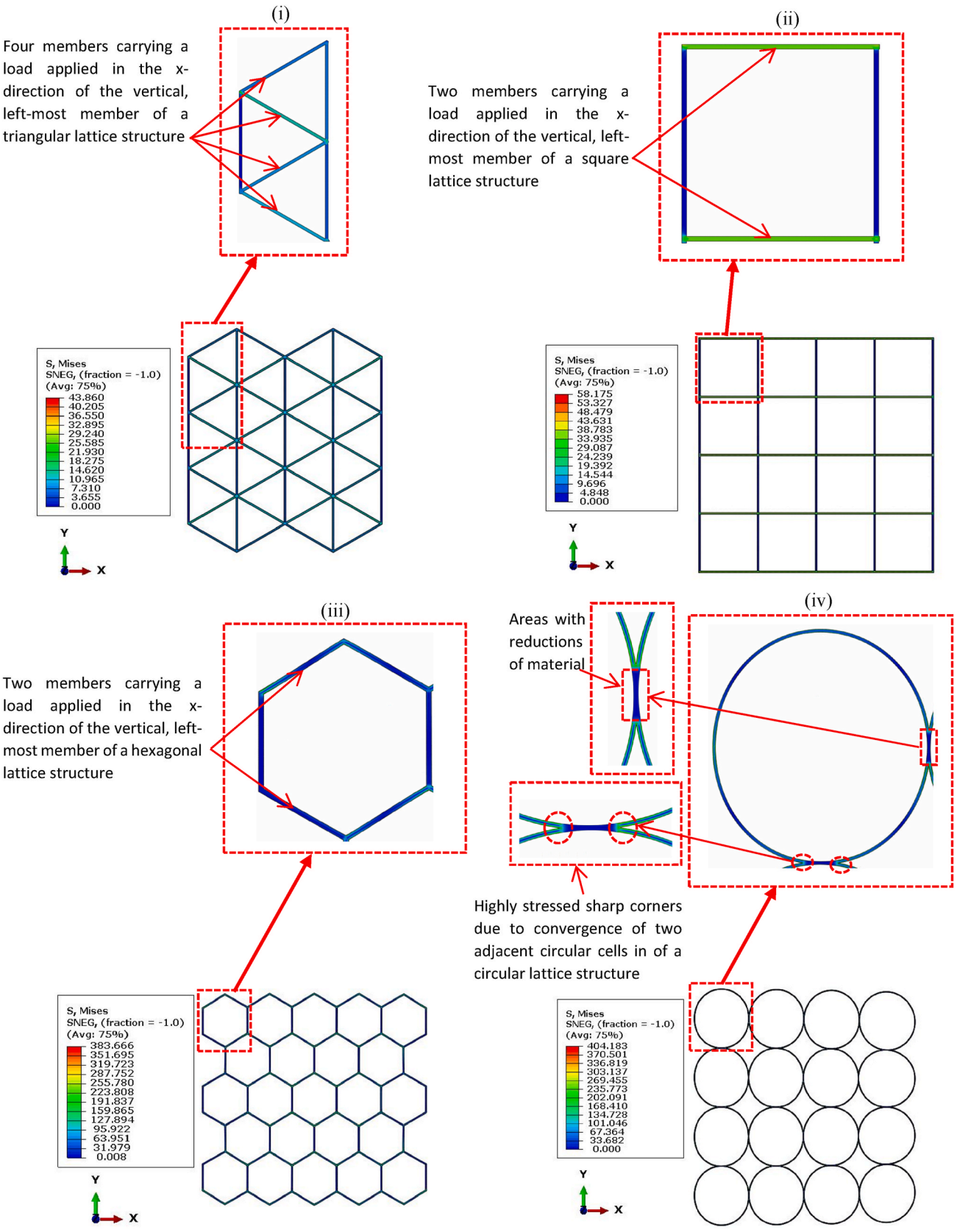


Fig. 10. The distribution of von Mises stresses in four different models of polygons for an applied load of 2000 N in the x-direction, highlighting (i – iii) members that transmit loads applied in the x-direction and (iv) areas of stress concentration.

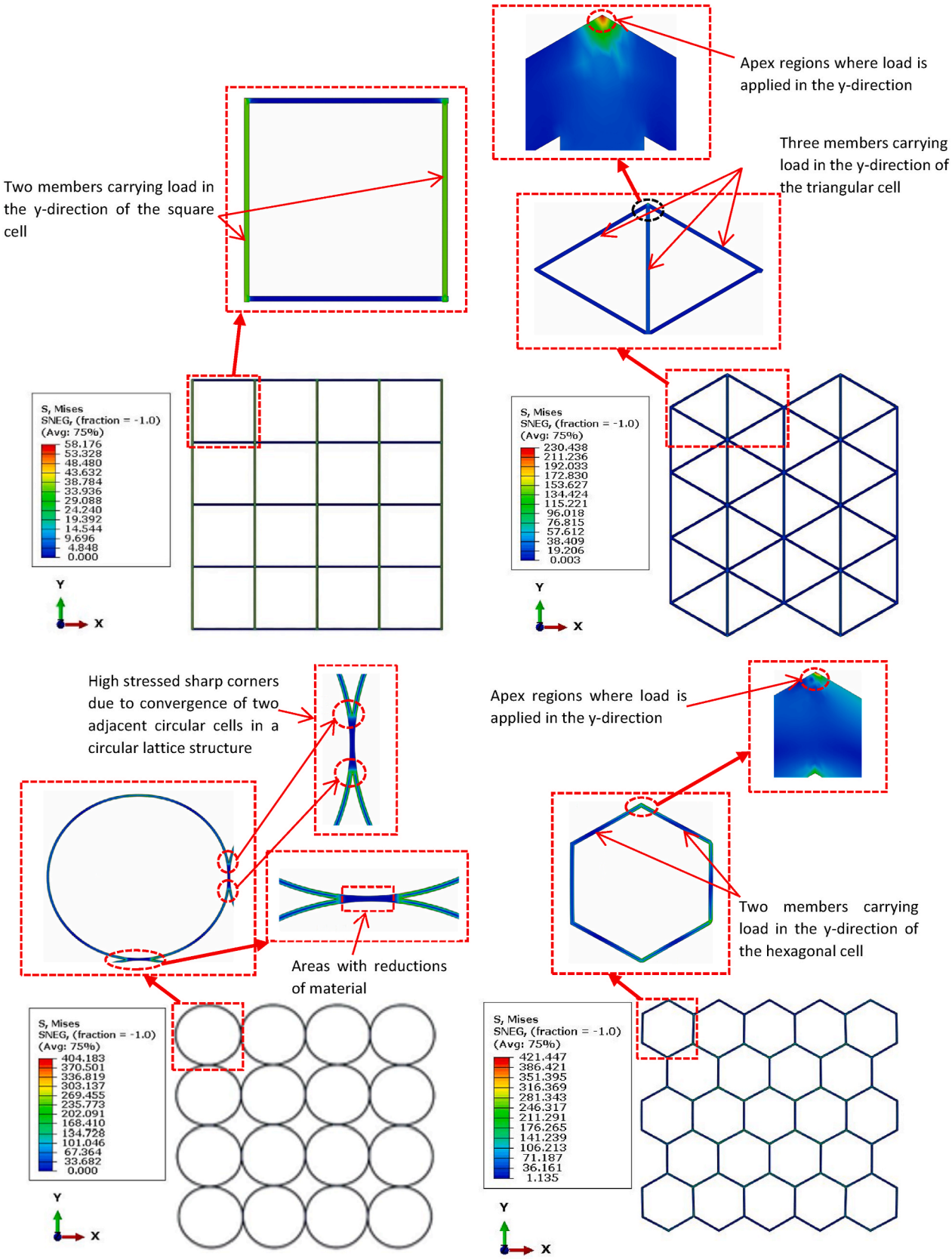


Fig. 11. The distribution of von Mises stresses in four different models of polygons for an applied load of 2000 N in the y-direction.

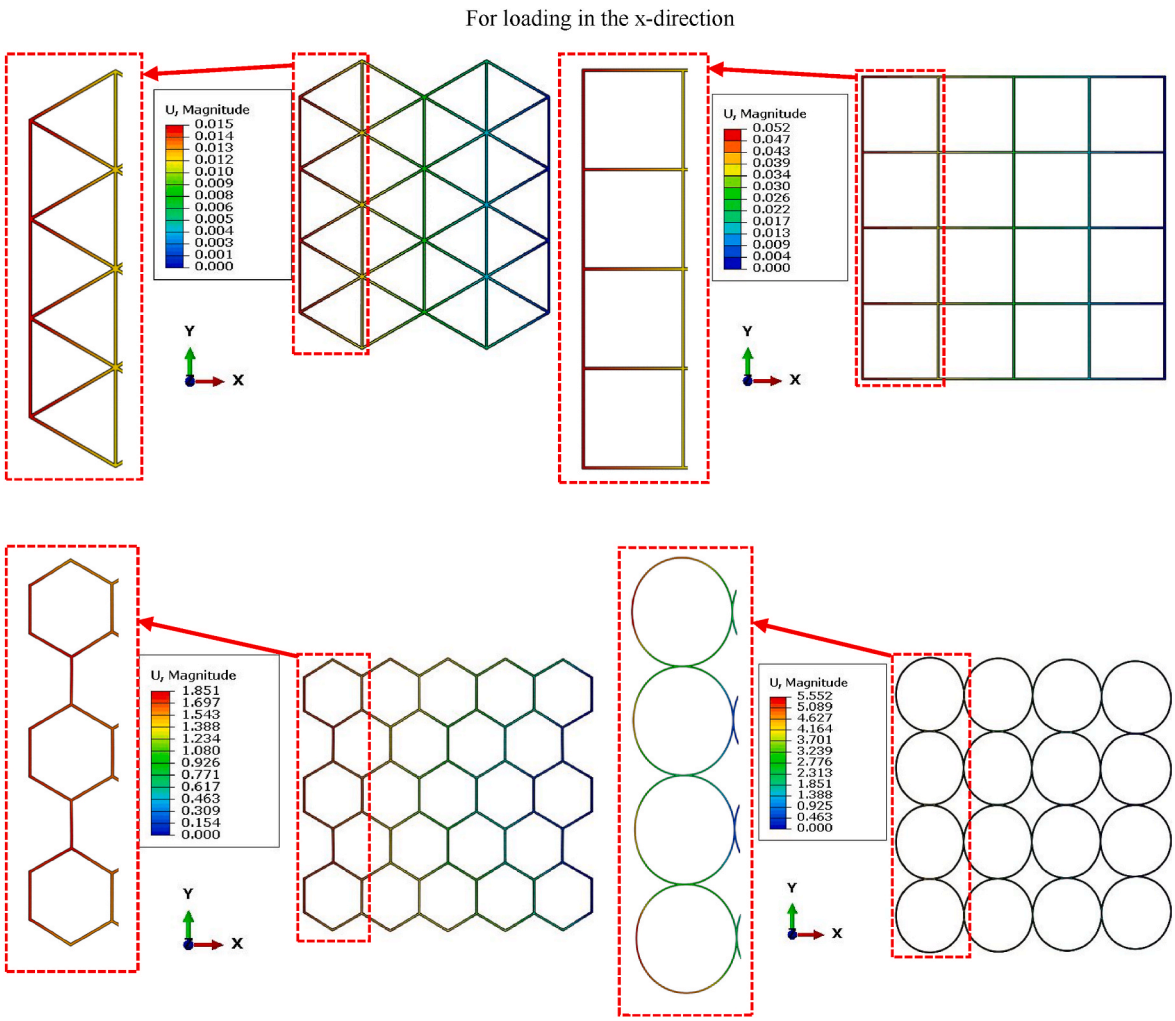


Fig. 12. Distribution of deflections for the four different models of polygons for an applied load of 2000 N in the) x-direction.

von Mises stress for a load of the same magnitude applied in the y-direction. Overall, therefore, the triangular polygon is the best choice of the four polygons modelled here.

Despite the foregoing choice of the best polygon, the hexagonal structure is by far the most widely researched [4,7,9,13,15,17,21–25], and is, therefore, used in the ensuing analysis to compare the results generated in this work and those from literature.

3.1.2. *Deformation behavior of HC models*

3.1.2.1. Bending and axial behaviour. Fig. 14 shows a comparison between the current simulations of HC structures and the ones reported in Refs. [17,23–25], with regard to their elastic deformation for loading along the x-direction. Identical elastic deformation shapes for both the theoretical [17,24,25] and current FEA results are observed. The HC model in the current FEA results was obtained using a uniaxial load, whereas the theoretical model in literature is based on a pressure load. Despite this difference in the type of loads applied to both models, there is no significant difference in the results. When the HC structure was exposed to a uniaxial compression load in the x-direction, both elastic bending and axial deformation of cell walls were initiated. The elastic deformation in the members of the structure occurred in the inclined members due to both axial compression and transverse bending, induced in them from the applied load acting along the x-axis, as shown in Fig. 15 (a). The elastic deformation mechanics of the inclined members shown in Fig. 15(b) are similar to what was observed in the theoretical models of references [17,25].

It is garnered from the current FEA results in Fig. 15(a) that the elastic deformation shapes resulted from one component stress load acting perpendicular ($F_{xp(Bending)}$) to and the other along ($F_{xa(Axial)}$) the member. This bending deflection and axial deformation of the inclined members contributed to the bulk movement of the upper and lower vertex regions in the y-direction (outwards), as demonstrated by the arrow attached to the vertical members leading from each one of the two circled regions. This behaviour is similar to the theoretical behaviour reported in Refs. [17,23–26]. Moreover, the vertices were observed to be highly stressed regions. These vertices of HC structures are, therefore, liable to fail due to the high stresses in these regions. This is similar to what was observed in Refs. [23,26]. It is therefore important to note that such regions are likely to fail first and should be considered carefully when analysing the behaviour of structural frames. It is also evident for all the unit cells that the vertical members have close to zero stresses, as also shown in Fig. 15(a). This is because the direct stresses are only transferred along the axial directions of the members, thus, in analysis of such structural frames, such members are considered to be redundant.

A similar numerical result for bending and axial deformation shapes to those discussed in Fig. 14 were obtained when the extruded HC shell was loaded along the y-direction as shown in Fig. 16(a). This is also similar to the behaviour for the existing theoretical model in literature shown in Fig. 16(b) [17]. However, the bulk movement of the vertex regions for this loading condition changed in direction. The vertices connecting the two inclined members are compressed into the cell, as

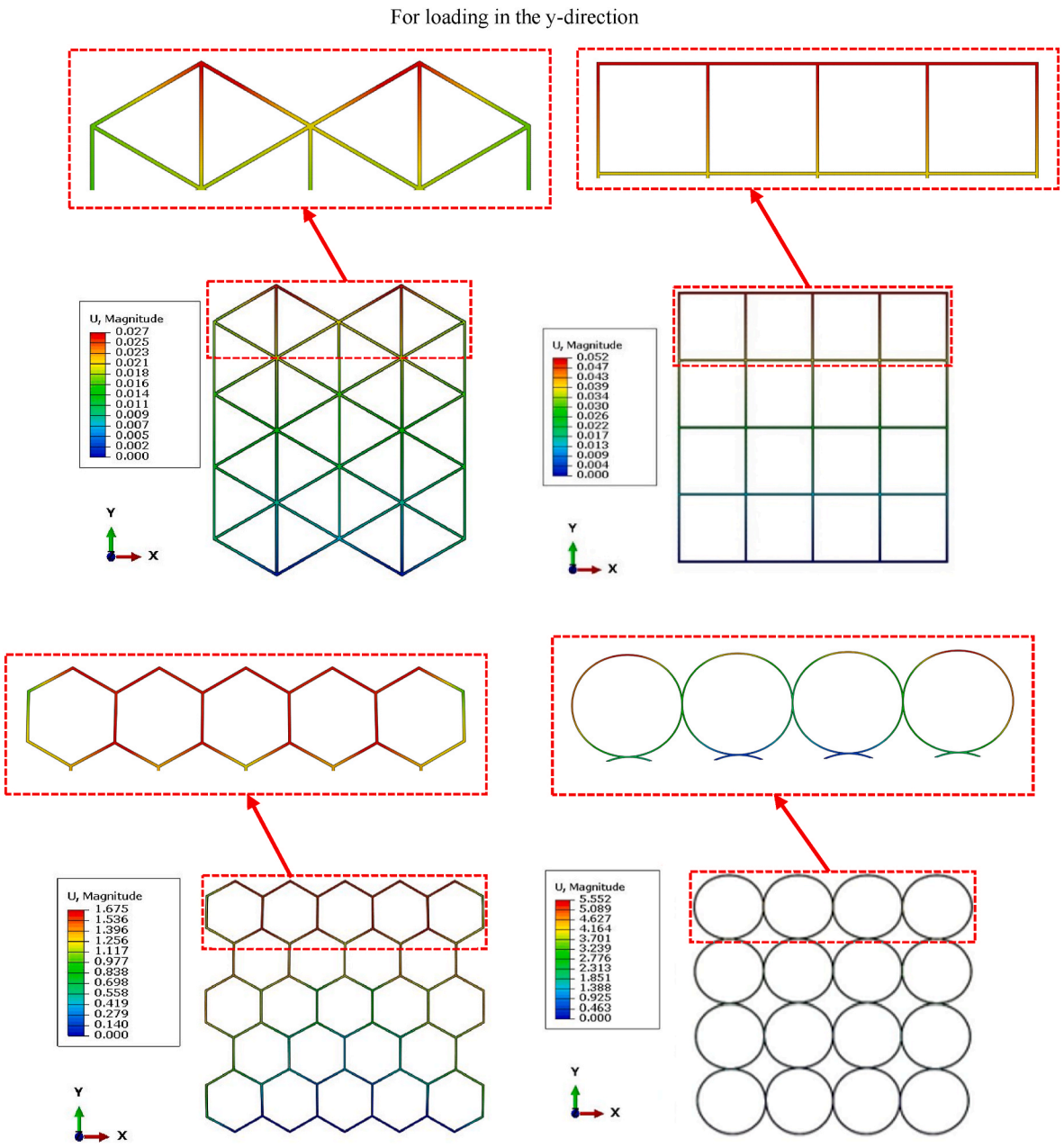


Fig. 13. Distribution of deflections for the four different models of polygons for an applied load of 2000 N in the y-direction.

Table 3
Ranking of different polygon structures by stress levels for loading in the x- and y-directions, from the lowest to the highest.

Type of polygon structure	Ranking for loading in the x-direction	Ranking for loading in the y-direction
Triangular	First	Second
Square	Second	First
Hexagonal	Third	Fourth
Circular	Fourth	Third

Table 4
Ranking of different polygon structures by deflection levels for loading in the x- and y-directions, from the lowest to the highest.

Type of polygon structure	Ranking for loading in the x-direction	Ranking for loading in the y-direction
Triangular	First	First
Square	Second	Second
Hexagonal	Third	Third
Circular	Fourth	Fourth

shown in Fig. 17, in contrast to their movement for the previous loading condition along the x-axis, where the vertices regions are pulled away from the centre of the cell. This is similar to what was observed in Refs. [17,23–26].

For efficient design and manufacture of engineering structures with complex behaviour, it is also important to consider the direction of loading. That this is so for the HC structure modelled here is evident from the contours of deflection for loads applied on it in the x- and y-directions shown in Figs. 18 and 19, respectively. The deflections for all thickness of members in the two figures were higher for the load applied in the x-direction, than in the y-direction.

The values of deflection for both load cases are seen in the two

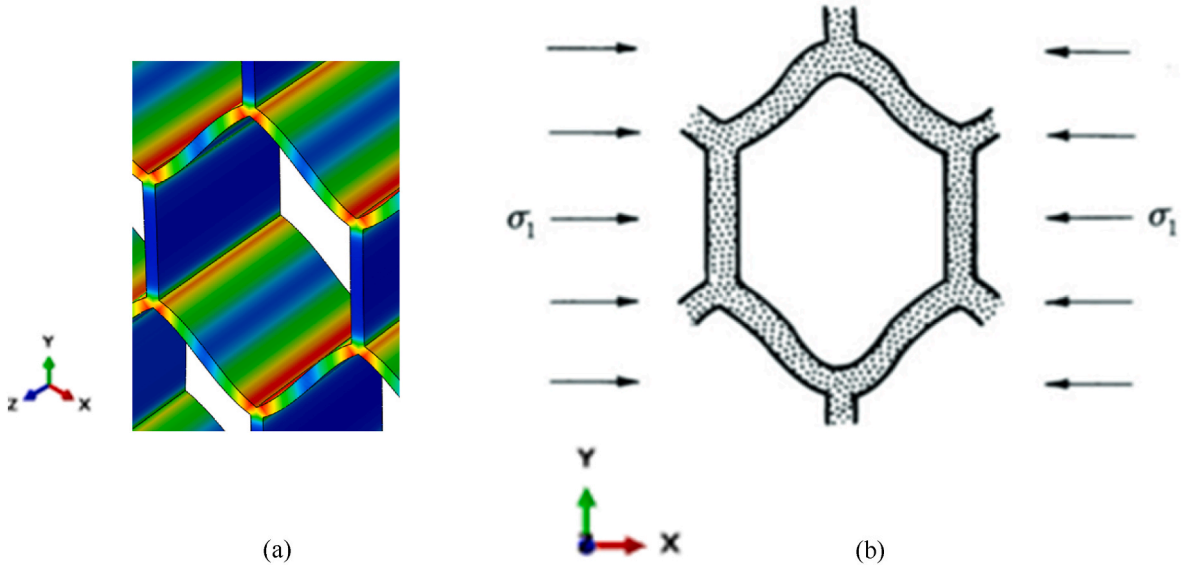


Fig. 14. Typical elastic deformations of (a) The current numerical model and (b) schematic of a theoretical model in literature [17,25] for a HC structure loaded along the x-direction.

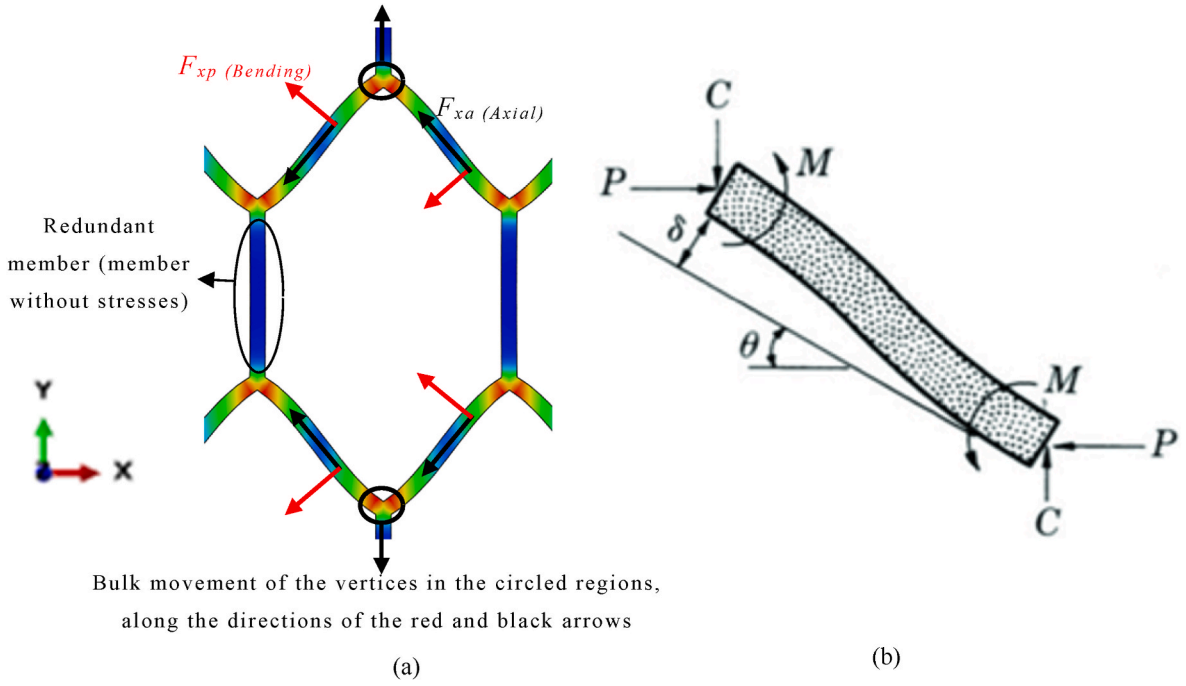


Fig. 15. The deformation mechanics for the (a) current numerical model, and (b) theoretical models [17,25], for loading in the x-direction.

figures to reduce with increasing wall thickness. The maximum values of deflection for the HC structure loaded in the x- and y-directions differed from the figures with a structure of 1 mm wall thickness by (18.16, 15.68, 14.12, 12.72, 11.37, and 10.28) percent and (12.92, 7.66, 18.06, 6.27, 13.39, and 15.81) percent, respectively. It is clear from these values, that the differences in the magnitudes of deflection obtained for different thicknesses of structures loaded in the x- and y-directions are significant, all being greater than 5%. Studies conducted in Refs. [17, 36–38] showed that percentage differences of more than 5% are significant.

The maximum values of deflection for the HC structure loaded in x- and y-directions, for different values of maximum elastic loads are presented in Table 5 and the values plotted in Fig. 20, using polynomial curves fits of order two, to facilitate a search for trends.

The maximum elastic loads were recorded for a value of stress experienced by the structure that is equal to the yield strength of its material. The curves in Fig. 20(a) show that the magnitudes of maximum elastic load applied to the HC model in the x- and y-directions have a directly proportional relationship to the wall thickness. The curves in Fig. 20(b), on the other hand, show that the corresponding values of deflection experienced by the HC model in the x- and y-directions are inversely related to the wall thickness. The correlation coefficients in the four graphs are less than one, showing that the relationship between variables is not coincidental. However, it is indicated in Refs. [39–41] that values above 0.95 are considered high correlation coefficients, which is shown for all four graphs.

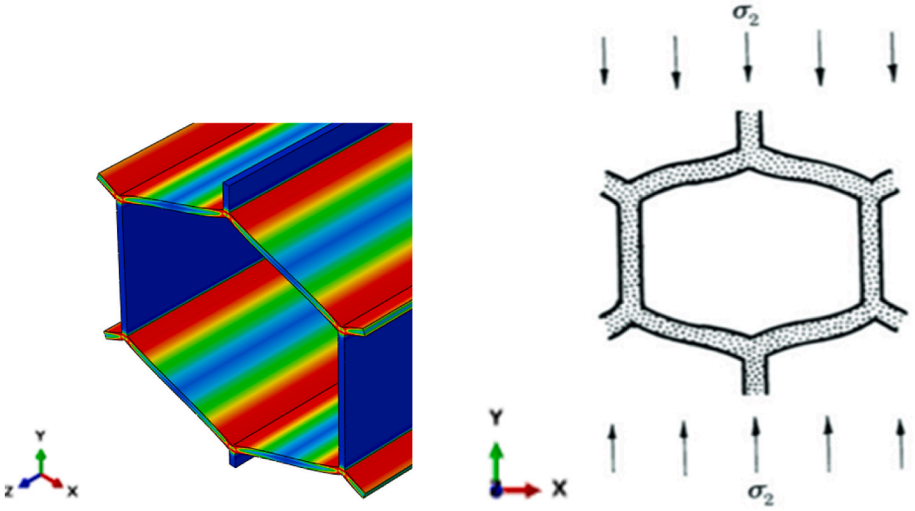


Fig. 16. Typical elastic deformations of (a) the hexagonal HC numerical model, and (b) image of an theoretical model in literature [17,25] of a honeycomb structure loaded along the y-direction.

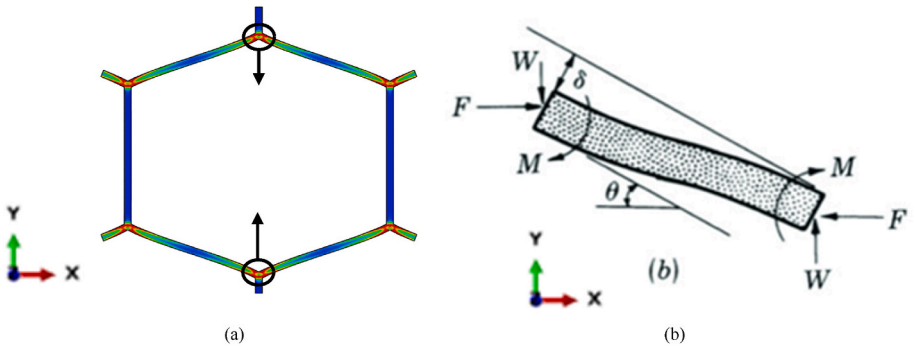


Fig. 17. The deformation mechanism obtained for the (a) current numerical model, and (b) theoretical models [17,25] loaded in the y-direction.

Curves for the maximum values of elastic load applied against corresponding values of deflection were generated from Fig. 20(a and b), with the results shown in Fig. 21.

It is clear from the curves in Fig. 21, that the maximum values of elastic load applied to the HC model in the x- and y-directions, have an inversely proportional relationship to the corresponding values of deflection experienced by the structure. Non-linearities are also observed in the curves depicted in the two figures (Figs. 20 and 21). The non-linearity observed in this figure and the previous one is due to how the applied load and corresponding deflections have dependence on the thickness of the walls of HC structures. The preceding assertion is a fact that is backed up by Equations (2) and (3), which clearly show that the stiffness and corresponding stress for an applied load are related by an exponential change to the thickness of the walls of HC structures. The stiffness and corresponding stress that result from a maximum elastic load grow by an exponential increase in the thickness of the walls of HC structures.

3.1.3. *Primary buckling behaviour*

The extruded HC shell models analysed here, with values of wall thickness of 1, 1.125, 1.25, 1.375, 1.5, 1.625, and 1.75 mm and the same value of length (L = 20 mm) had (t/L) values less than 0.1 and are thus, all slender. Therefore, Euler's theory of buckling was adopted in their analysis. The values of critical loads (P_c) and related stresses for each thickness were then calculated using Euler's Equation (5) and Equation (6), respectively, and are presented in Table 6.

$$P_c = \frac{\pi EI}{l_e^2} = \frac{\pi Ebt^3}{12l_e^2} = Bt^3 \tag{5}$$

$$\sigma_c = \frac{P_c}{A} = \frac{Bt^3}{bt} = Ct^2 \tag{6}$$

where, symbol P_c stands for the critical buckling load, E Young's modulus, I area moment of inertia, b width, l_e equivalent length, A cross-sectional area, b breadth, t thickness, and B and C constants, all of the wall plates/shells of the structure.

For uniaxial loading in the z-direction, the calculated values in Table 6 show that the HC shell model will fail by elastic buckling, ahead of yielding, when wall thicknesses (1, 1.125, and 1.25) mm are used. This is because the calculated buckling stresses at these values of wall thickness, for the calculated values of critical loads, are all less than the yield stress of the material for the shell walls of 790 MPa. The von Mises stress contours of the HC shell model are shown in Fig. 22, and the values of critical loads and their corresponding buckling stresses are presented in Table 7.

It is observed from the results in Fig. 22 and Tables 7 and in contrast to the previous results from analytical modelling, that for all the different wall thickness of the HC structure, loads well in excess of the yield stress of the material are required for buckling to occur. It is likely

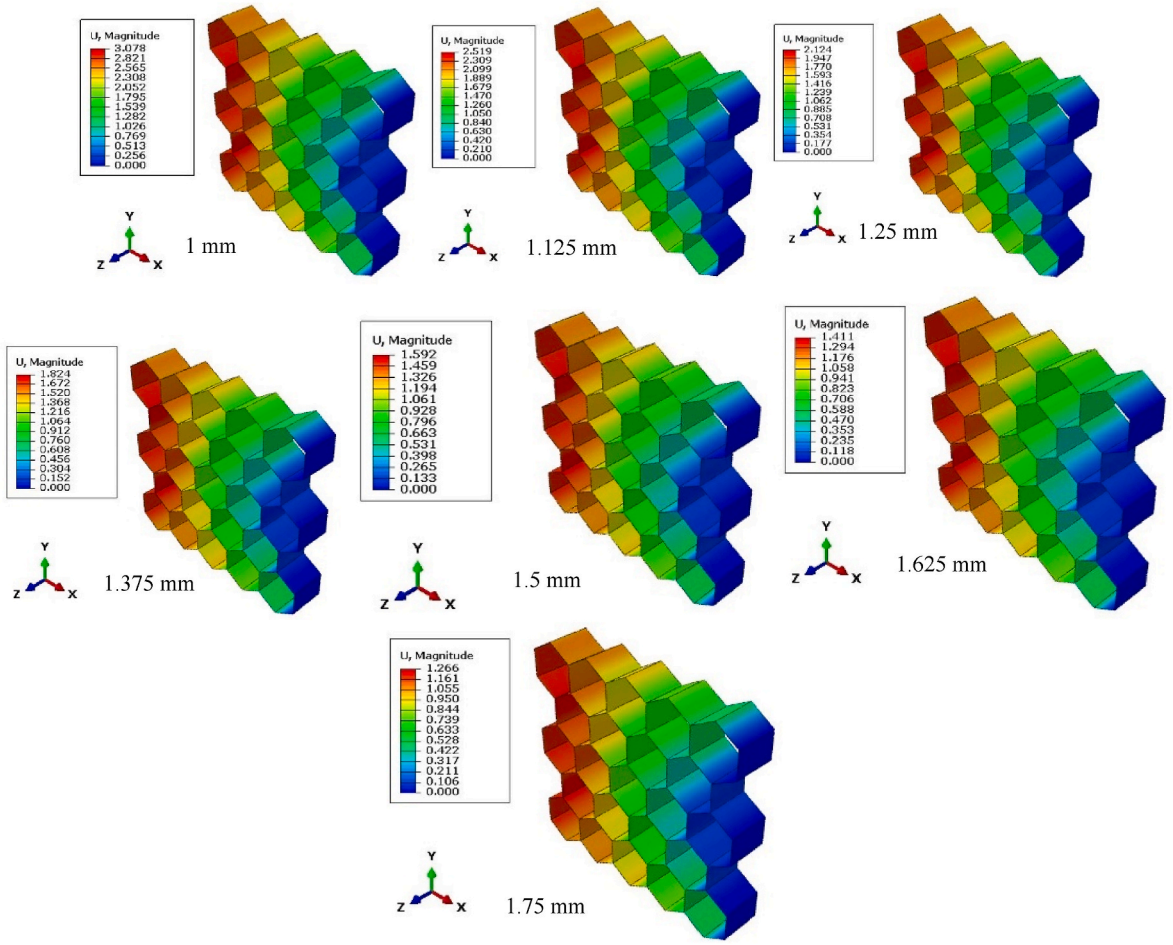


Fig. 18. Numerical results of deflection for HC structures of different wall thickness loaded in the x-direction.

that these very high values of stress that are well above the yield stress of the material, could have resulted from combination of axial and bending stresses for the HC model. The HC shell model had higher stresses at the mid-span regions of the plates because of the occurrence of greater bending stresses at the mid-spans of its plates. It is likely that buckling would not occur below the yield stress of the material because the shells in the HC model had a restraining effect against one another, causing the structure to stiffen.

In the numerical modelling carried out here, the critical loads causing the first buckling mode to occur were determined by multiplying the applied nominal load (1 KN) by the eigenvalue for the model. This is because the potential buckling strength of a structure in the ABAQUS software used in this work, is predicted via eigenvalue analysis. The results of numerical and analytical modelling shown in Tables 6 and 7 are plotted in Fig. 23.

The curves in these two figures show that the critical load and related stresses are close to directly proportional (with correlation coefficients greater than 0.95 correlation) to the third and fourth power of the thickness of the shells/plates, respectively, for loading in the z-direction. The curves in these two figures are consistent with those reported in Refs. [17,25].

The buckled shapes for primary buckling of both the numerical and analytical models are similar, as shown in Fig. 24.

The values of deflection of the HC shell model in this figure are given relative to a value of 1 for the highest deflection, as is normal for linear buckling, given the fact that its subroutine is set to only detect the presence and absence of buckling. Because linear buckling analysis does not provide absolute values of deflection, it cannot facilitate comparisons of the deflections of models with different thicknesses, which demands use of an alternative approach. This does not diminish the value of undertaking linear buckling because in most cases the primary need is only to determine the presence or absence of buckling. It is clearly shown in Fig. 24 that the faces adjacent to one another for the HC model buckled in different directions, inwards and outwards. Furthermore, the points of maximum deflection occur at the mid-points of the plates. Fig. 24 also shows that there is a higher degree of buckling towards the centre than at the peripheries of the plates. This is a function of the intercellular restrain that is higher towards the edges than towards the centre of the plates.

The veracity of the conclusion made regarding the restraining effect of the hexagonal cells against one another for the HC shell model, was tested using a unit hexagonal cell, a plate with vertical fixed sides, and another plate without vertical fixed sides, respectively, all pinned at their bottom edges. This was done to determine whether the critical buckling loads recorded in the preceding analysis that were above the material's yield stress are attributable to the restraining effect of adjacent shells in the model or not. Fig. 25 shows the results in terms of von Mises stress and deflections, that were obtained for these models, all which had plate thickness of 1 mm.

The three different models shown in this figure required critical loads of (0.141, 0.014, and 0.001) MN, for a unit hexagonal cell, a plate with fixed vertical sides, and a plate without fixed sides, respectively for buckling to occur. The values clearly show that stiffness and therefore, critical load does increase with increasing restrain of the plates.

It is also observed in Fig. 25(a) that the plate without constrained vertical sides buckled below the material's yield stress in contrast to the other two models. Therefore, it can be deduced that the adjacent shells in a HC structure have a stiffening effect on the plates, and therefore, the

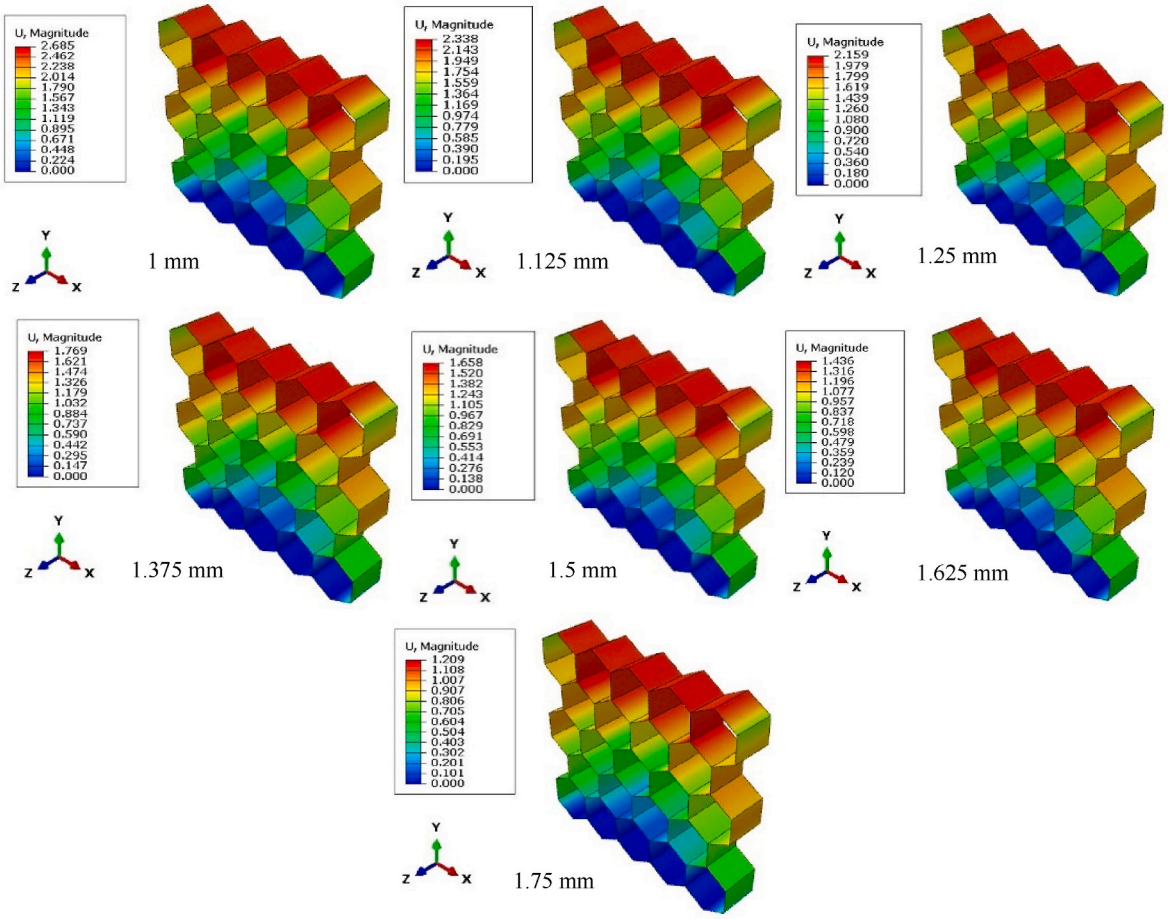


Fig. 19. Numerical results of deflection for HC structures of different wall thickness loaded in the y-direction.

Table 5
Values of load applied to a HC structure in the x- and y-directions and the corresponding values of deflection.

Loading in the x-direction		
Wall thickness (mm)	Maximum value of elastic load (N)	Corresponding value of deflection (mm)
1	3600	3.078
1.125	4500	2.519
1.25	5600	2.124
1.375	6300	1.824
1.5	7000	1.592
1.625	7800	1.411
1.75	8500	1.266
Loading in the y-direction		
Wall thickness (mm)	Maximum value of elastic load (N)	Corresponding value of deflection (mm)
1	3500	2.685
1.125	4350	2.228
1.25	5480	2.159
1.375	6100	1.769
1.5	6880	1.658
1.625	7640	1.436
1.75	8390	1.207

observed values of stresses of the HC structure at buckling that are well above the yield stress of the material for HC models.

The results for linear buckling clearly cannot yield values of deflection and therefore, the need to explore nonlinear buckling analysis. This method employs a non-linear geometric analysis to model the transition from direct deformation to buckling and to eliminate the observed limitation of linear buckling analysis through other features as well.

In practical buckling, there is no such thing as a perfectly straight structure, perfect constraint, or ideal application of load. There is also no completely homogenous material composition [42]. In practice, all of these factors contribute to small eccentricities and changes that attract offset axial stress. This, in turn, causes offset moments, which induce even more eccentricity. Buckling will not occur in a very stable real structure, but eccentricities will build until instability arises in an intermediate typical model of the structure [43]. Fig. 26 shows a contour plot of the von Mises stress. The von Mises stress contours in this figure clearly show that the HC shell model went plastic before it reached its critical buckling load of 1.46 MN. This image is also accompanied by ones of non-linear buckling of an extruded single hexagonal cell, as well as plates with and without restrained vertical sides, similar to those shown in Fig. 25.

Non-linear analyses of the chosen shell models of 1 mm thickness show that their use could result in more accurate and detailed behaviour. The results also show that shell models had a large area where stresses higher than the yield stress of the material were experienced (areas with grey contours), except for the plate without restrained vertical sides. This means that a large percentage of the material used to build the structures had deformed plastically before the structure buckled. It is important to note that such HC parts cannot be adopted for normal engineering applications. This is because the structure has far exceeded its design constraints. Therefore, the restraining effect of hexagonal cells walls against one another is also confirmed by the results of nonlinear buckling, and it is evident from Fig. 26 that the critical buckling load is reduced for decreasing intercellular wall restrain. With

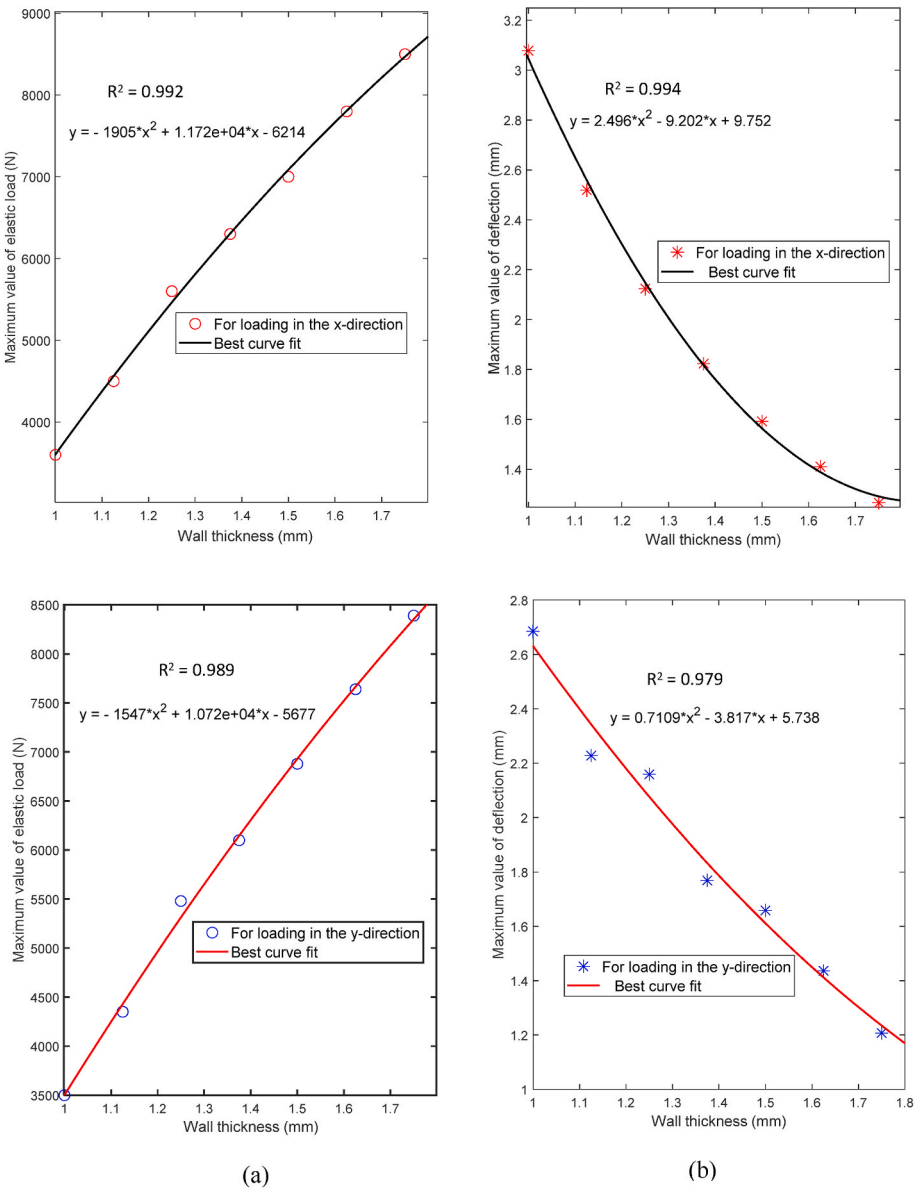


Fig. 20. Curves with (a) maximum applied loads and (b) maximum deflections experienced in the x- and y-directions of the HC model at different values of thickness (t) of its members.

reference to the HC model, the load decreased to (0.0930, 0.0145, and 0.0033) MN for the unit hexagonal cell, plates with and without restrained vertical sides, respectively.

One of the advantages of using non-linear analysis over linear analysis is that it is able to take account of plastic deformation. The simulation for nonlinear analysis of buckling was run using the Johnson-Cook Model that is built into ABAQUS/CAE. It is common and simple to use the Johnson-Cook (J-C) model to describe the isotropic flow properties of metals and metallic alloys during deformation due to plasticity. Plastic deformation of the Ti6Al4V(ELI) HC structures under nonlinear buckling in this work, was investigated using the set of J-C parameters obtained from literature shown in Table 8 [44].

where the symbol A denotes the yield stress, B the strain hardening factor, C the dimensionless strain rate hardening coefficient, and n and m the strain hardening and thermal softening exponents, respectively. Fig. 27 shows the contours of plastic strain for the same models as in Fig. 26, except for the plate model without restrained vertical sides, for the reason that it buckled within the elastic phase of deformation.

It is observed in Fig. 27, that the shell models had the highest plastic strains occurring at the mid-span locations of the hexagonal cell. The foregoing results of non-linear analysis of buckling clearly demonstrate that the structure is more likely to fail first by axial compression than by buckling.

3.2. *Effects of the t/L ratio on the effective stiffness of HC structures*

For out-of-plane loading of the HC shell model, the corresponding relationships between the yield strain and the ratios t/L and $(t/L)^3$ were plotted in Fig. 28(a and b), respectively.

The yield strains were obtained for HC structures of different wall thicknesses loaded to maximum elastic stresses close to the yield stress of the selected material of 790 MPa. The curves in the figure are similar to what was observed in Ref. [45]. The highest strain resulting from each model was evaluated to determine if the subsequent FE analysis would be limited to maximum stress values that the HC shell structure can bear before the material surpasses yield stress. To relate strain to Equation (2), the arising strains were plotted against the relevant ratios of t/L and $(t/L)^3$. For Ti6Al4V, whose values of mechanical properties were used in

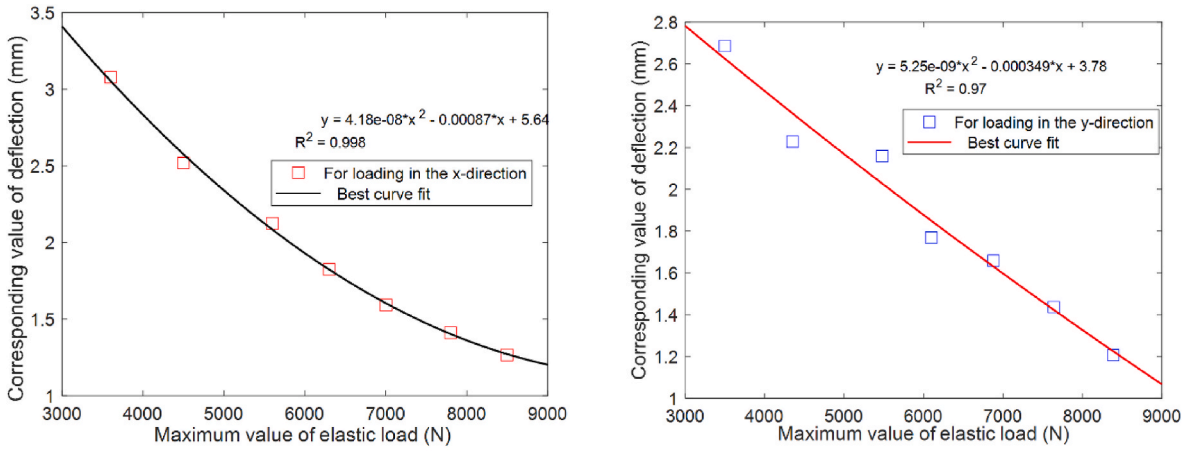


Fig. 21. Curves of the (a) x-, and (b) y-direction maximum applied loads versus maximum corresponding deflections.

Table 6
Calculated values of critical buckling loads and buckling stresses for the hexagonal extruded shell model, with different wall thicknesses.

Shell wall thickness t (mm)	Critical buckling load P_c (MN)	Buckling stress σ_c (MPa)
1	0.049	373.533
1.125	0.083	614.815
1.25	0.114	760
1.375	0.151	915.152
1.5	0.197	1094.444
1.625	0.250	1282.051
1.75	0.312	1485.714

numerical modelling in this work, a yield strain value of 0.699% is obtained from Hooke's Law based on values of yield stress and stiffness of 790 MPa to 113.8 GPa [46]. With a safety factor of 1.5, this value reduces to 0.446%. These are the strains that should be targeted when using the material as intended for lightweight parts in applications. The FE models, however, recorded elastic strains that are more than the allowable yield strain (0.699%). It is likely that this resulted from the effects of bulk movement of the structure and therefore, deflection on top of deformation.

The curves in Fig. 28, which are generated using numerical models, show that strains decrease nonlinearly as the thickness of the walls of HC structures increases. This is further confirmed by the analytical model in Equations (2) and (3). The observation made in Fig. 28 is due to the fact that the corresponding strains to either the stiffness or stresses are inversely related to the exponential change in the thickness of HC structure walls. In Fig. 28(a), the nonlinearity in the strains is detected for the last three plotted points, but in Fig. 28(b), the nonlinearity increased to the last five points. This is with the mathematical models, which clearly show that the degree of exponential change in the thickness of the walls of HC structures has a direct influence on how strains decrease with increasing wall thickness. The curves in Fig. 28 also show that the strains are slightly greater for both ratios when the HC model is loaded in the y-direction as opposed to the x-direction. This is due to the fact that loading in the x-direction occurs at the face, but loading in the y-direction occurs at the apex regions. When compared to the former, the latter loading case generates slightly higher stressed areas.

The effect of the t/L ratio on the stiffness of HC structures is now discussed, based on Equation (2). At first, the thickness of HC cell walls was varied from 1 to 1.75 mm, with a corresponding variation of the t/L ratio from 0.05 to 0.0875. Fig. 29 shows the relation between the moduli ratio and the corresponding t/L ratios from the numerical and analytical results.

It is evident in Fig. 29 that in the current FE model the effective stiffness increased non-linearly as the t/L ratio increases. The mathematical model in equation (2) confirms this by showing how the stiffness of HC structures increases exponentially with wall thickness. The FE results plotted in this figure agree well with those from the analytical models of Gibson and Ashby [17], with the largest difference being 2.2 $\times 10^{-4}$ and 5.9 $\times 10^{-4}$ for the x- and y-direction loading, respectively. This is because stiffnesses of structural frames such as the HCs are dependent on the t parameter used, for constant values of L. By increasing the value of t, the structural frame experiences an increase in structural stiffness. The stiffness of the structure increases as the thickness increases because the material is able to resist deformation and bending more effectively. The relationship between thickness and stiffness is fundamental to structural mechanics and is described in numerous mathematical models, including the Euler-Bernoulli beam theory and the Timoshenko beam theory [33]. It is noted that the analytical models overestimated the effective stiffness for the two ratios. This could be because the analytical models in Ref. [17] did not consider the stiffening effects at the fixed nodes/vertices that was demonstrated earlier in Fig. 22.

3.3. Comparison of implemented simulation/modelling in the current work and experimental results in literature

A comparative analysis of the numerical models implemented in the present work and experimental results on Ti6Al4V hollow structures in literature can provide useful insights into the accuracy and reliability of predictive approaches in capturing the mechanical behaviour of such complex parts.

The greater part of the documented work in literature for Ti6Al4V hollow structures has been conducted on the strut-based and triply periodic minimal surface (TPMS)-based designs for hollow shapes [1,47,48]. This is because Ti6Al4V strut-based hollow designs are easy to construct and are used for numerous aerospace applications [48], and Ti6Al4V TPMS-based hollow designs are more amenable to biomedical applications [47]. Experimental results obtained from the literature [22–25,27], are consistent with those of the numerical models in the present work for various polygon shapes, both concurring that vertices are regions of high stresses for hollow structures. Antolak-Dudka et al. [49] experimented on Ti6Al4V HC parts under static and dynamic compression loads. Their work highlighted the fact that the vertices or nodes typically fail first under compression loading. It must be noted that this pattern of failure is not only applicable to hollow structures

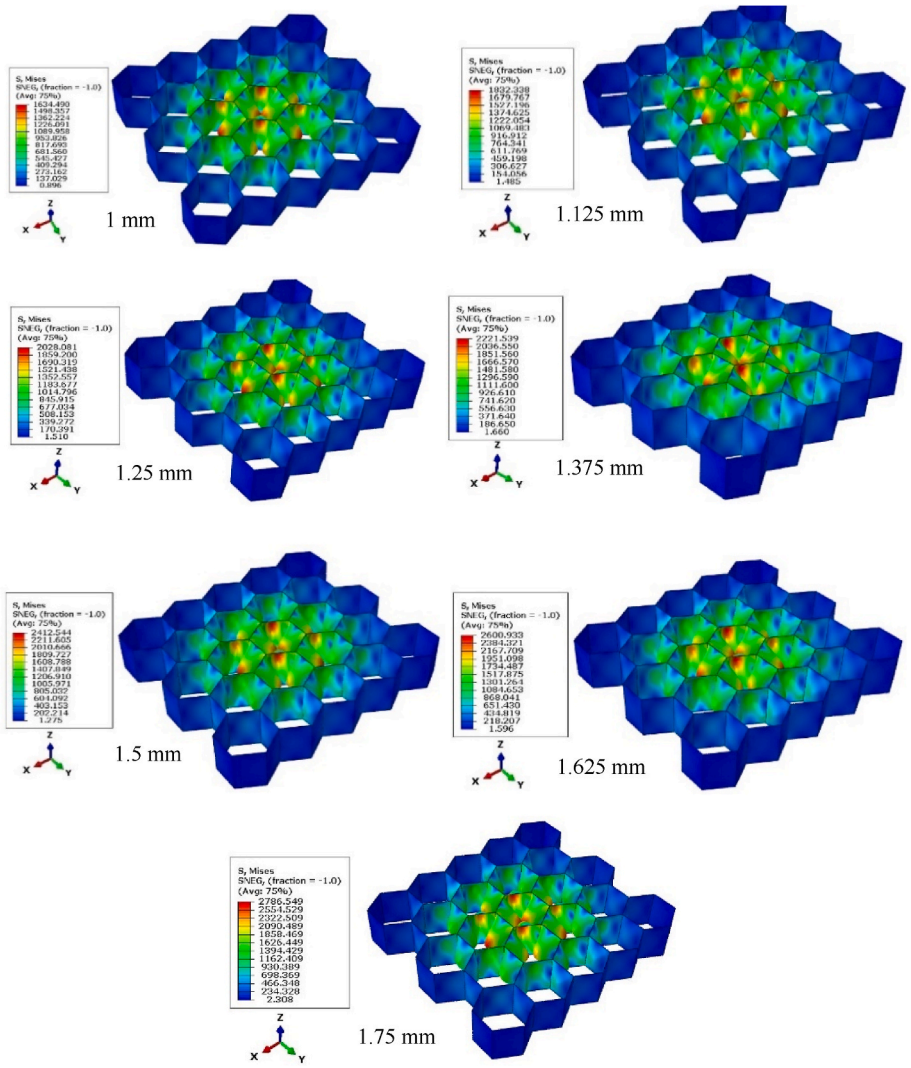


Fig. 22. Distribution of von Mises stresses at the buckling stresses of the HC model for different shell thickness.

Table 7
Numerical values of critical buckling loads and the corresponding stresses at these loads for the hexagonal extruded shell model with different wall thicknesses

Shell wall thickness *t* (mm)	Critical buckling load (MN)	Buckling stress (MPa)
1	1.233	1634.490
1.125	1.748	1832.338
1.25	2.386	2028.081
1.375	3.160	2221.539
1.5	4.079	2412.544
1.625	5.156	2600.933
1.75	6.401	2786.549

built of Ti6Al4V, but also to those constructed using other alternative materials [17,22], as the phenomenon is a function geometry and not materials [4,7,11]. Generated numerical models in the present study also show that the most critical direction of loading hollow shapes is the one in which loads are applied directly at points of sharp changes of geometry such as apexes where vertices converge. The authors were not able to identify with experimental validation of this last phenomenon, as the literature available on polygon hollow shapes [13,14,17,22–26,30,34,35] was on loads applied transversely to the members of these structures. In the present work, it has been shown that numerically modelled triangular hollow structures had the lowest deflection for loading at apexes, as they had more members transferring load than the other polygon structures modelled in this work. In order of ranking, triangular hollow structures were shown in the present work to be followed by square, hexagonal, and finally circular hollow shapes. This is an important finding, as such ranking of various polygon structures with respect to deflection is unavailable in literature. Experimental confirmation of this ranking forms part of future planned work. In addition, it is noted that of the numerous studies reviewed [1,10,12,14,18,19,21,22,27,31,42,47,49], none provides a rationale for the selection of different types of hollow shapes but rather proceed to use the selected shapers for analysis in engineering applications without considering their rank in terms of their mechanical properties.

According to the numerical models generated in the present work, the predominant deformation behaviour of HC structures is the bending of the walls. This concurs with what has already been analytically and experimentally confirmed in numerous studies [17,21–26]. Gibson et al. [25] validated HC mechanical models experimentally via compression tests on metal and moulded silicone rubber parts. Their experimental results reproduced the mechanical properties of HC parts consistent with the developed theory [17]. Choy et al. [50] performed compression experiments on Ti6Al4V HC parts built using selective laser sintering (SLM) and confirmed a similar predominant deformation mechanism. The values of deflection resulting from the current numerical models for the HC structure under out-of-plane loads in both the x- and y-directions,

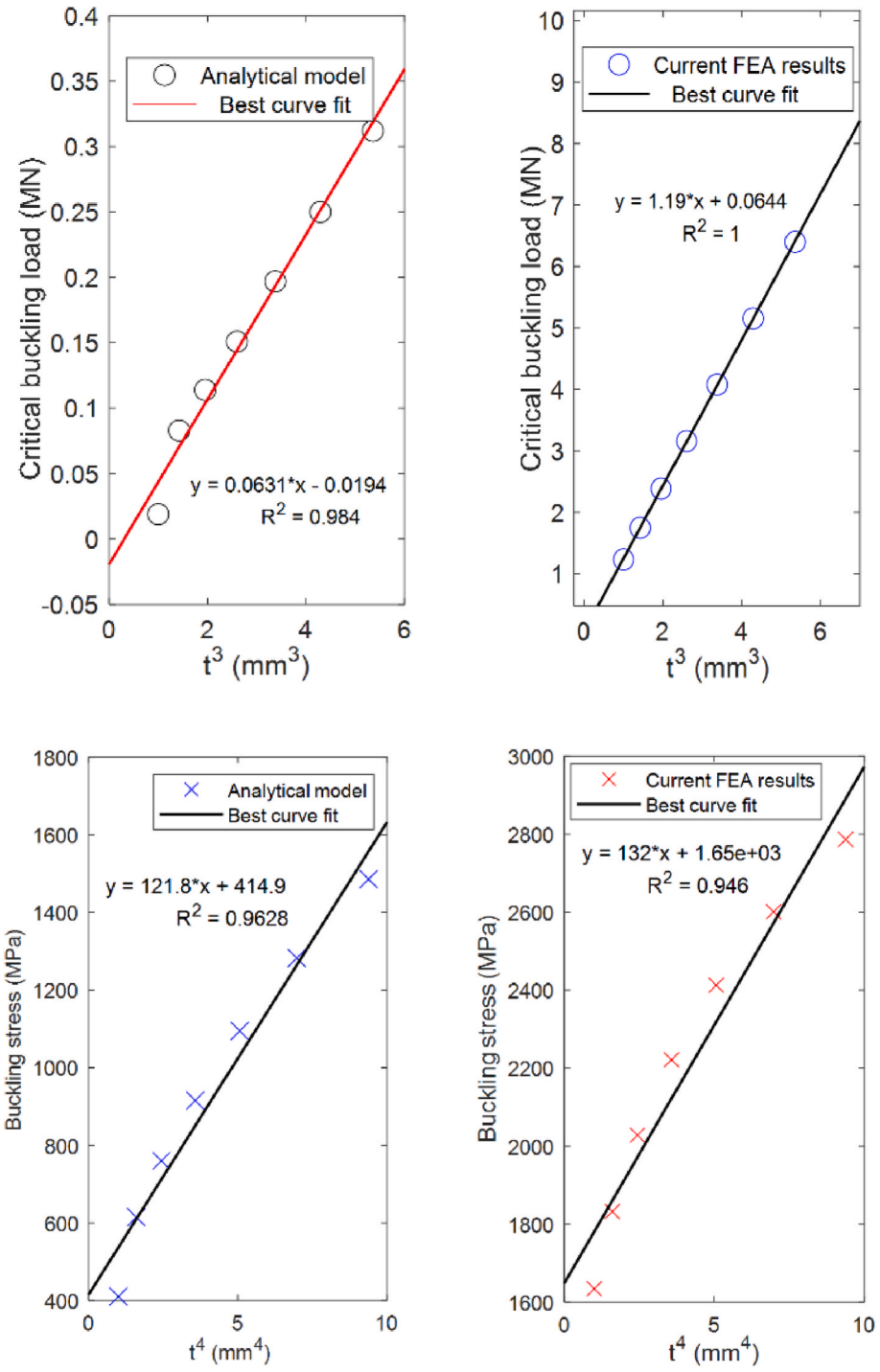


Fig. 23. Critical buckling loads and stresses versus the wall thickness of the numerical HC model loaded in the z-direction.

separately, diminish with increasing wall thickness. This is consistent with numerous studies that have demonstrated with experimental results that the stiffness of hollow structures is improved by increasing their wall thickness [17,21,49,50]. Hussein et al. [51] modelled the elastic behaviour of laser PBF Steel 304L HC parts with different cell wall thicknesses (from a range of 0.2–0.5 mm) while retaining a fixed cell size of 3.97 mm. Obadimu and Kourousis [52] then validated the findings of Hussein et al. [51], with results that supported the correlation that exists between geometrical parameters and mechanical properties.

The numerical models implemented in the present work for HC parts that are subjected to in-plane loads generated values of stress exceeding the yield stress of Ti6Al4V, suggesting that failure by axial compression would occur ahead of buckling failure, as highlighted in numerous studies [9,17,18,21,26,29,42]. It must be highlighted, however, that the greater part of studies currently available in literature focuses solely on HC parts made of materials with moduli of elasticity that are lower than the value for Ti6Al4V, such as alloys of aluminum [20,21,28,53–56]. Therefore, experiments are clearly required to validate the exact values of deflection and stress obtained in the numerical models of the Ti6Al4V polygon shapes generated in the present work. The numerical results for linear buckling generated in the present work show that the largest stress levels occur at mid-span regions of the plates used to construct the HC shell models. This agrees with the findings in Ref. [57]. Furthermore,

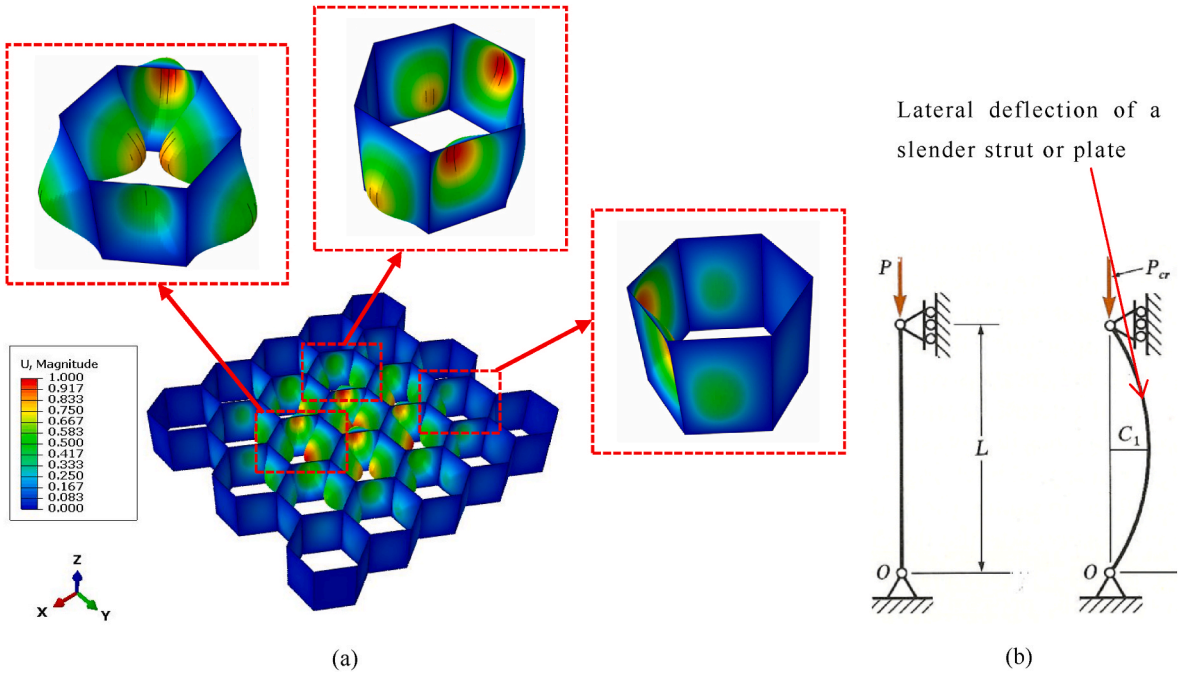


Fig. 24. Current numerical and existing theoretical elastic buckling first mode shapes on a HC structure with uniaxial loading acting in the *z*-direction.

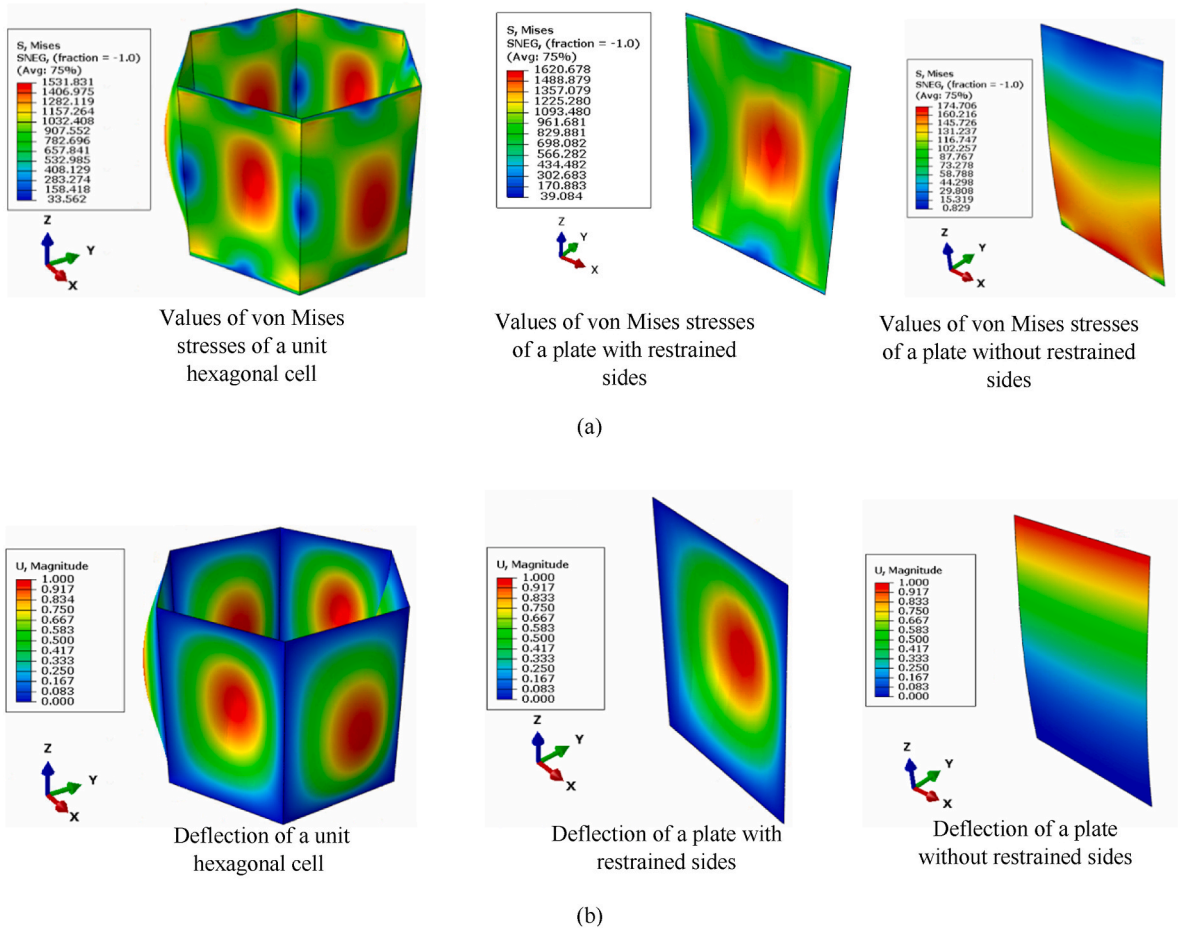


Fig. 25. A buckled unit hexagonal cell, and plates with and without vertical fixed sides from the left to the right, respectively, showing (a) von Mises stress, and (b) deflection contours.

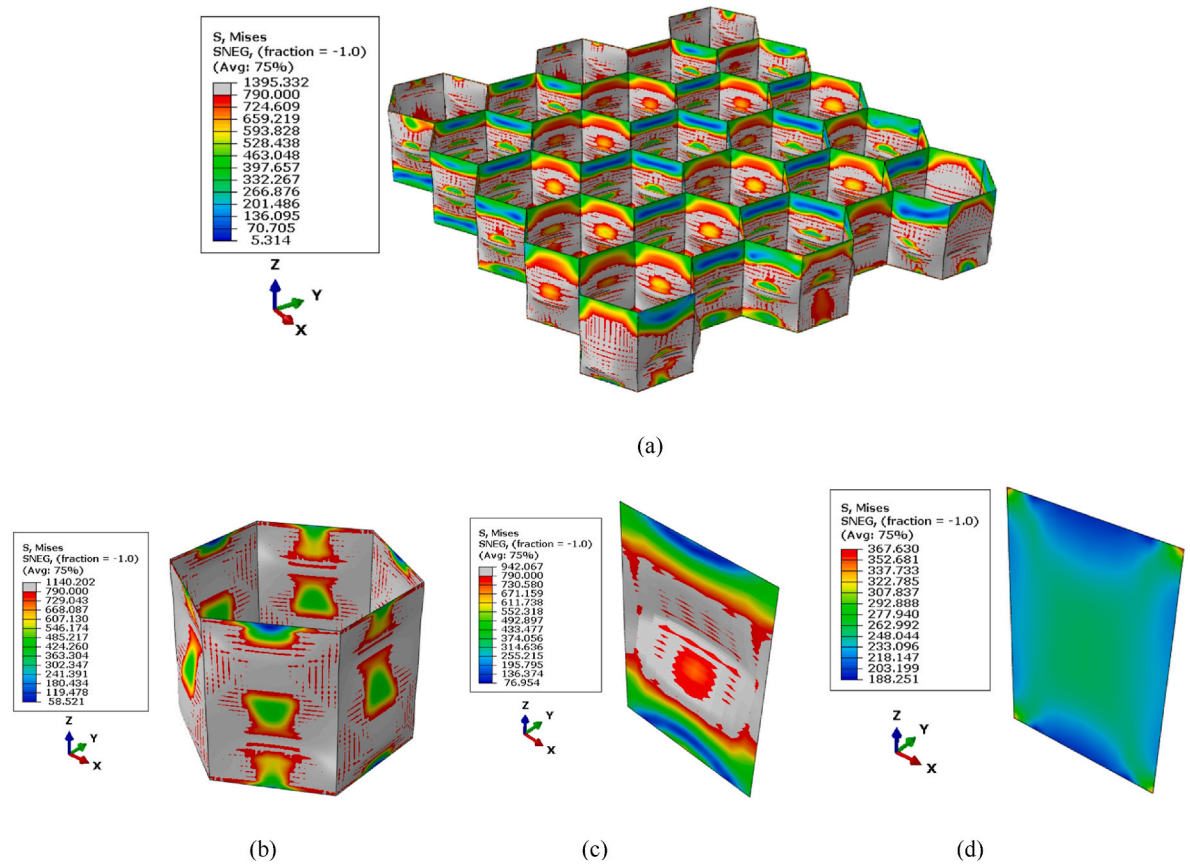


Fig. 26. Von Mises stress contours of shell models of wall thickness 1 mm, including (a) the HC, (b) the unit hexagonal cell, (c) the plate with restrained vertical sides, and (d) the plate without restrained vertical sides.

Table 8
Set of J-C model parameters [44].

Parameter for J-C model	A (MPa)	B (MPa)	*n*	C	*m*
Lee & Lin [44]	782.7	498.4	0.28	0.0028	1

the numerically generated shapes after deflection of the HC plates correlate with those produced in Refs. [57,58]. The numerical analyses for linear and nonlinear buckling carried out in the present work showed that the HC model's adjacent shells exhibit a restraining effect against each other, resulting in the stiffening of the structure. There appears to be a knowledge gap with regard to experimental validation of the aforementioned restraining effect, which calls for future experimentation to solve this shortfall of information. The prediction based on the numerical models for analysing the effect of wall thickness on the effective stiffness of the HC shell in this work correlates well with the results of experiments done in Ref. [35]. Silva et al. [59] also examined how design and manufacturing parameters affected the compressive behaviour of 3D-printed polymer lattice structures. Their results tie in with those of the present work of increasing density and thus the mechanical properties of the hollow structures with increasing thickness of the struts.

3.4. Extending the simulation and modelling implemented here to other metallics and their various applications

Implementation of the current simulation and modelling procedure to include other alloys could prove useful for developing and optimising hollow structures with specific applications. This method provides insights into the mechanical properties of hollow shapes and thus improves the basis for developing structures that respond effectively to specific applications. For the purpose of developing innovative and effective designs, the numerical models developed here for Ti6Al4V hollow structures could be tailored and extended to other alloys.

Tungsten alloys are used in shielding radiation applications due to their extremely high density compared to Ti6Al4V, particularly in the medical and nuclear sectors [60]. Tungsten alloy hollow structures could be built to be lightweight while maintaining good shielding. The effects of radiation on materials could be factored into numerical models, and the shielding efficacy of different hollow shapes evaluated. Tungsten [61] and nickel-based [62] alloys have good thermal stability and mechanical strength compared to Ti6Al4V. The high thermal conductivity of tungsten and nickel-based alloys allows them to be designed as hollow shapes for efficient heat transfer [63]. Heat conduction and thermal stress distribution within different hollow shapes, as well as their mechanical performance, could be simulated using numerical models. These hollow shapes are often used in aeronautical propulsion systems and defense applications in harsh conditions [63,64]. Additionally, the tungsten alloy's good thermal conductivity results in it being good for heat sinks in electronics [61,63]. Building hollow structures with such material could assist with heat dissipation. The use of simulations and modelling allows for the evaluation of cooling efficiency for the different hollow shapes and optimisation of their design in accordance with specific uses. Tungsten alloys are susceptible to particular corrosive conditions [61], whereas Ti6Al4V is corrosion-resistant [46]. Numerical models could mimic corrosion behaviour and predict how different hollow shapes reduce or further aggravate corrosion effects. The complete densification of tungsten alloys during AM is difficult due to its high melting point and heat conductivity [63]. The potential for porosity and partial densification could be reduced by hollow structure design since there will be less material to

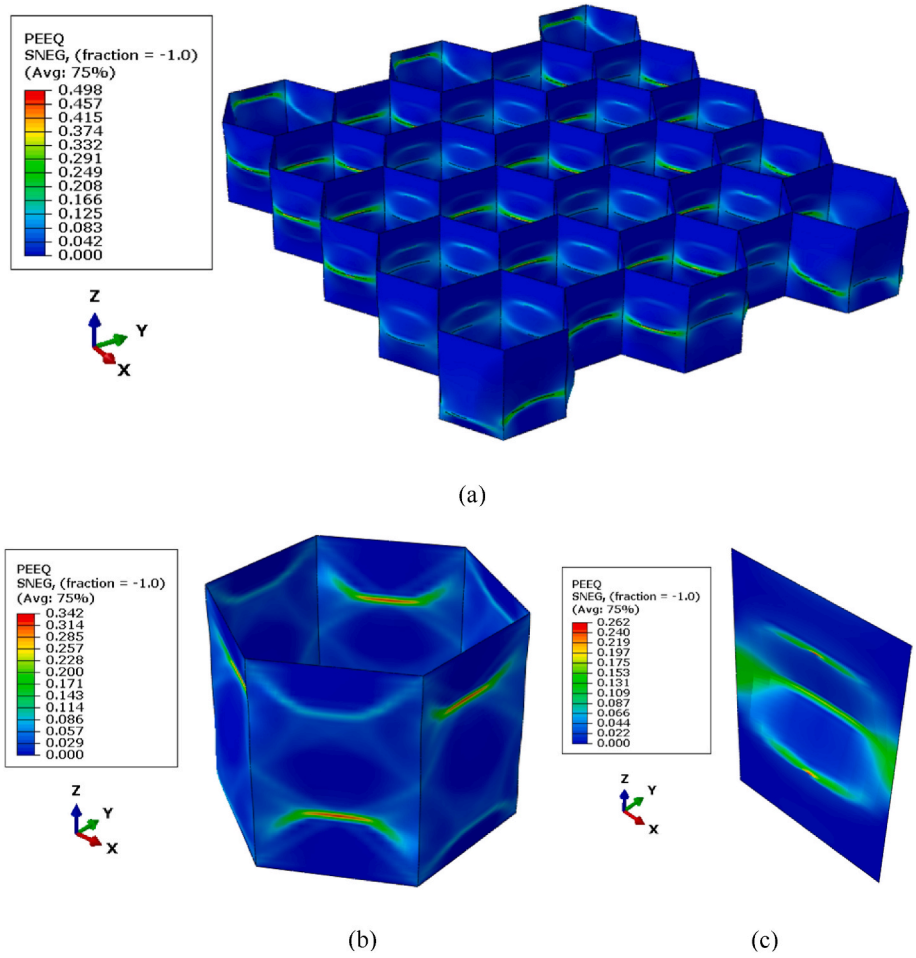


Fig. 27. Plastic strain contours for the shell models of wall thickness 1 mm, including (a) the HC, (b) the unit hexagonal cell, and (c) the plate with restrained vertical sides.

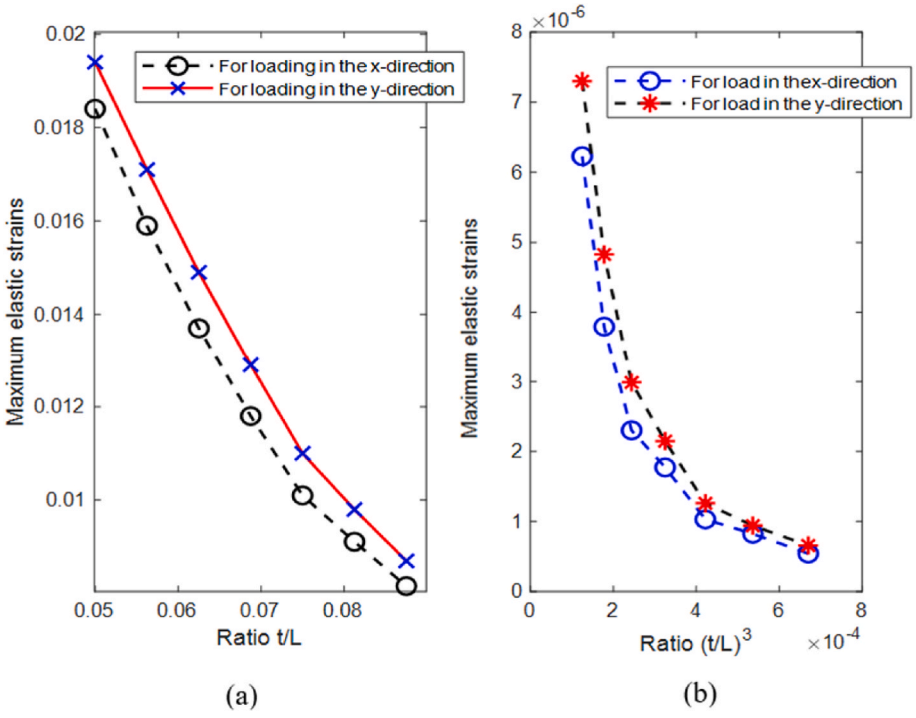


Fig. 28. Numerical results for elastic strains against the ratio (a) t/L and, (b) $(t/L)^3$ for the HC model.

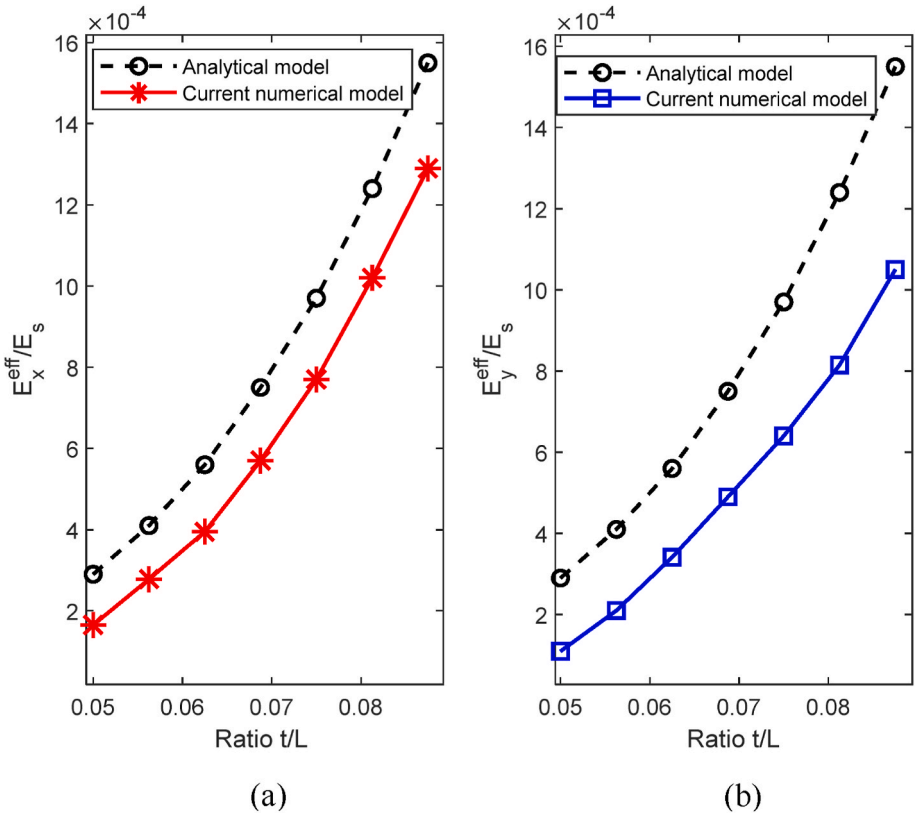


Fig. 29. The effective stiffness of the regular hexagonal honeycomb, with out-of-plane load: Comparison between current FE predictions and analytical model predictions by Gibson and Ashby [17].

solidify. This is because hollow geometry can minimise porosity while improving density by reducing the gradients in temperature and also assisting in uniform cooling [63]. Better control over solidification cooling rates could be achieved with hollow structures. Simulation and modelling must therefore be extended to examine how different tungsten alloy hollow shapes influence microstructure control in regard to minimizing or increasing grain growth, resulting in increased or decreased mechanical properties, respectively.

Copper alloys are popular for their electrical conductivity which is high compared to Ti6Al4V. Hollow shapes are useful for designing connectors, conductive pathways, and electronics cooling components [65]. Numerical models could assist in the design of different copper alloy hollow shapes in order to improve the transfer of heat and flow of electrical current. Furthermore, their high thermal conductivity results in copper being a better material for heat exchangers [65]. Hollow structures could further enhance the efficiency of heat transfer. Different hollow shapes could be implemented in simulation and modelling to predict their influence on the distribution of temperature and drop of pressure across a structure. Copper alloys are corrosion-resistant and have been used for decades in applications related to plumbing. Pipes, fittings, and fluid distribution systems are designed as hollow structures [66]. Better structural integrity and flow properties could be predicted by employing numerical models of different hollow shapes built using copper alloys [67]. Integrating copper hollow shapes as fins into current designs of pyramid-shaped solar still has the prospect of improving heat transfer, evaporation, and condensation rates, ultimately leading to the production of distilled water. To maximise benefits whilst minimizing drawbacks, the design and location of such copper structures could be studied carefully. Incorporating the numerical models developed here in such a design could assist in the optimisation of design and understanding of the complex relationship between the copper hollow shapes and the functionality of the solar still.

By systematically comparing the mechanical behaviour of other alloy hollow shapes against Ti6Al4V hollow structures using the implemented numerical models, researchers could arrive at well-versed design decisions that account for performance, cost, and application requirements. Such an approach would in turn allows researchers to design hollow structures of each material for their specific applications, optimising performance while taking material properties and the limits of their mechanical properties into account.

4. Conclusion

At the onset of this work, analysis of area-coverage and material-usage was done for a number of polygons to determine the best one amongst them. Planar and extruded HC shell models were subsequently modelled numerically, to determine the best configuration to use in the investigation that followed. This was followed by FE simulation for various polygon structures to determine the best polygon structure under uniaxial compression loads. The thickness of a hexagonal structure was adjusted to investigate the influence of the t/L ratio on buckling behavior and effective stiffness in the in-plane and out-of-plane direction, respectively. The study yielded the following conclusions:

- Based on tessellation analysis, the hexagonal polygon turns out to be the best design option of the four polygons tested, since it offers both large area-coverage and minimal use of material.
- The small difference of about 3.71% in the maximum von Mises stresses of planar and extruded hexagonal models, justified using the planar model instead of the more complex extruded model in order to reduce computing resources.
- The disparities observed at the vertices of the extruded hexagonal shell could result in the development of topologies with no congruence at the vertices in topology and shape optimisation and therefore, constrain further numerical modelling.

- The triangular polygon recorded the lowest deflections for the same magnitude of load applied in each direction, separately. It also recorded the lowest maximum von Mises stress in the x-direction and the second lowest maximum von Mises stress in the y-direction, for the same magnitude of load applied in both directions, separately. As a result, the triangular polygon is considered the best alternative of the four polygons studied here.
- The FE HC shell model achieved bending deflection and axial deformation shapes that are consistent with literature, for out-of-plane loading.
- The critical buckling loads for HC numerical shell models of different thicknesses generated von Mises stresses that were higher than the material's yield stress. This is in contrast to the case for analytical modelling, in which the critical loads generated von Mises stresses for the first three HC shell models of (1, 1.125 and 1.25) mm wall thickness were below the yield stress of the material used here. The critical buckling loads were observed to increase as the ratio t/L grew. The HC shell numerical model was significantly stiffened due to the restraining action of hexagonal cells against one another.
- Non-linear analysis has the advantage of accounting for plastic deformation, which is not possible with linear analysis. The degree of plastic deformation is higher at the mid-points of hexagonal cell plates. Therefore, the structure may be suggested to fail due to axial compression first, then buckling.
- The numerical and analytical models for the HC shell structure, both showed that the effective stiffness increased with the t/L ratio.

Future research should focus on experimentation for all of the differing polygon structures computationally modelled in this work in order to confirm the obtained results. Moreover, in order to reduce stress concentrations and increase stiffness, topology and shape optimisation at the vertices and size optimisation of the polygon structures should be investigated, respectively.

Author contribution statement

All the authors were involved in conceptualization, methodology, investigation, software, formal analysis, validation, writing, reviewing, and editing of this article.

Declaration of competing interest

The authors declare that they have no known competing financial interests or personal relationships that could have appeared to influence the work reported in this paper.

Data availability

Data will be made available on request.

Acknowledgements

Funding: This work is based on research supported by the South African Research Chairs Initiative of the Department of Science and Technology, and the National Research Foundation of South Africa (Grant No. 97994), and the Collaborative Program in Additive Manufacturing (Contract No. CSIR-NLC-CPAM-21-MOA-CUT-03).

References

[1] J. Noronha, J. Rogers, M. Leary, E. Kyriakou, S.B. Inverarity, R. Das, M. Qian, Ti-6Al-4V hollow-strut lattice materials by laser powder bed fusion, Addit. Manuf. 72 (2023), 103637.
[2] R. Soni, R. Verma, R.K. Garg, V. Sharma, A critical review of recent advances in the aerospace materials, Mater. Today: Proc. (2023). https://doi.org/10.1016/j.intermet.2015.10.024.
[3] M.M. Abdel-Mottaleb, S. Salunkhe, B. Alqahtani, Mechanical properties of titanium alloys additive manufacturing for biomedical applications, Advances in Metal Additive Manufacturing (2023) 219–231.
[4] A. Du Plessis, C. Broeckhoven, I. Yadroitsava, I. Yadroitsev, C.H. Hands, R. Kunju, D. Bhate, Beautiful and functional: a review of biomimetic design in additive manufacturing, Addit. Manuf. 27 (2019) 408–427.
[5] Z. Zhang, Z. Li, S. Pan, X. Chai, Enhanced strength and high-temperature wear resistance of Ti6Al4V alloy fabricated by laser solid forming, J. Manuf. Sci. Eng. 144 (11) (2022), 111011.
[6] B. Jin, Q. Wang, L. Zhao, A. Pan, X. Ding, W. Gao, X. Zhang, A review of additive manufacturing techniques and post-processing for high-temperature titanium alloys, Metals 13 (8) (2023) 1327.
[7] M. Benedetti, A. Du Plessis, R.O. Ritchie, M. Dallago, S.M.J. Razavi, F. Berto, Architected cellular materials: a review on their mechanical properties towards fatigue-tolerant design and fabrication, Mater. Sci. Eng. R Rep. 144 (2021), 100606.
[8] M. Sarraf, E. Rezvani Ghomi, S. Alipour, S. Ramakrishna, N. Liana Sukiman, A state-of-the-art review of the fabrication and characteristics of titanium and its alloys for biomedical applications, Bio-design and Manufacturing (2021) 1–25.
[9] X. Zhang, Y. Wang, B. Ding, X. Li, Design, fabrication, and mechanics of 3D micro-/nanolattices, Small 16 (15) (2020), 1902842.
[10] D. Da, J. Yvonnet, L. Xia, M.V. Le, G. Li, Topology optimization of periodic lattice structures taking into account strain gradient, Comput. Struct. 210 (2018) 28–40.
[11] C. Pan, Y. Han, J. Lu, Design and optimization of lattice structures: a review, Appl. Sci. 10 (18) (2020) 6374.
[12] X. Yu, J. Zhou, H. Liang, Z. Jiang, L. Wu, Mechanical metamaterials associated with stiffness, rigidity, and compressibility: a brief review, Prog. Mater. Sci. 94 (2018) 114–173.
[13] L. Yang, O. Harrysson, H. West, D. Cormier, Mechanical properties of 3D re-entrant honeycomb auxetic structures realized via additive manufacturing, Int. J. Solid Struct. 69 (2015) 475–490.
[14] F.W. Zok, R.M. Latture, M.R. Begley, Periodic truss structures, J. Mech. Phys. Solid. 96 (2016) 184–203.
[15] A. Bührig-Polaczek, C. Fleck, T. Speck, P. Schüler, S.F. Fischer, M. Caliaro, M. Thielen, Biomimetic cellular metals—using hierarchical structuring for energy absorption, Bioinspiration Biomimetics 11 (4) (2016), 045002.
[16] M. Helou, S. Kara, Design, analysis, and manufacturing of lattice structures: an overview, Int. J. Comput. Integrated Manuf. 31 (3) (2018) 243–261.
[17] L.J. Gibson, M.F. Ashby, Cellular Solids: Structure and Properties, second ed., Cambridge University Press, New York, 1997.
[18] H.N. Wadley, N.A. Fleck, A.G. Evans, Fabrication and structural performance of periodic cellular metal sandwich structures, Compos. Sci. Technol. 63 (16) (2003) 2331–2343.
[19] J. Banhart, Manufacture, characterisation and application of cellular metals and metal foams, Prog. Mater. Sci. 46 (6) (2001) 559–632.
[20] P. Kędzierski, R. Gieleta, A. Morka, T. Niezgoda, Z. Surma, Experimental study of hybrid soft ballistic structures, Compos. Struct. 153 (2016) 204–211.
[21] X. Zhang, H. Zhang, Z. Wen, Experimental and numerical studies on the crush resistance of aluminum honeycombs with various cell configurations, Int. J. Impact Eng. 66 (2014) 48–59.
[22] T. Goldmann, W.C. Huang, S. Rzepa, J. Džugan, R. Sedláček, M. Daniel, Additive manufacturing of honeycomb lattice structure—from theoretical models to polymer and metal products, Materials 15 (5) (2022) 1838.
[23] S. Malek, L. Gibson, Effective elastic properties of periodic hexagonal honeycombs, Mech. Mater. 91 (2015) 226–240.
[24] L.J. Gibson, The Elastic and Plastic Behaviour of Cellular Materials, University of Cambridge, 1981.
[25] L.J. Gibson, M.F. Ashby, G.S. Schajer, C.I. Robertson, The mechanics of two-dimensional cellular materials, Proc. Roy. Soc. Lond. 382 (1982) 25–42.
[26] W.E. Warren, A.M. Kraynik, Foam mechanics: the linear elastic response of two-dimensional spatially periodic cellular materials, Mech. Mater. 6 (1) (1987) 27–37.
[27] L. Yan, Y. Chen, F. Liou, Additive manufacturing of functionally graded metallic materials using laser metal deposition, Addit. Manuf. 31 (2020), 100901.
[28] W. He, L. Yao, X. Meng, G. Sun, D. Xie, J. Liu, Effect of structural parameters on low-velocity impact behavior of aluminum honeycomb sandwich structures with CFRP face sheets, Thin-Walled Struct. 137 (2019) 411–432.
[29] P.S. Ghatage, V.R. Kar, P.E. Sudhagar, On the numerical modelling and analysis of multi-directional functionally graded composite structures: a review, Compos. Struct. 236 (2020), 111837.
[30] S. Gonella, M. Ruzzene, Homogenization and equivalent in-plane properties of two-dimensional periodic lattices, Int. J. Solid Struct. 45 (10) (2008) 2897–2915.
[31] P. Szymczyk, V. Hoppe, G. Ziółkowski, M. Smolnicki, M. Madeja, The effect of geometry on mechanical properties of Ti6Al4V ELI scaffolds manufactured using additive manufacturing technology, Arch. Civ. Mech. Eng. 20 (1) (2020) 1–13.
[32] B. Vrancken, L. Thijs, J.P. Kruth, J. Van Humbeeck, Heat treatment of Ti6Al4V produced by selective laser melting: microstructure and mechanical properties, J. Alloys Compd. 541 (2012) 177–185. Vrancken, B., Thijs, L., Kruth, J. P., & Van Humbeeck, J. (2012). Heat treatment of Ti6Al4V produced by Selective Laser Melting: Microstructure and mechanical properties. Journal of Alloys and Compounds, 541, 177-185.
[33] J. Case, A.H. Chilver, Strength of Materials: an Introduction to the Analysis of Stress and Strain, Elsevier, 2013.
[34] M.I. Chibinyani, T.C. Dzogbewu, M. Maringa, A.M. Muiruri, Reduced order topology optimisation of a planar honeycomb defined by a linear elastic Ti6al4V (ELI) material model, S. Afr. J. Ind. Eng. 33 (3) (2022) 299–317.

[35] Y. Chen, H. Hu, In-plane elasticity of regular hexagonal honeycombs with three different joints: a comparative study, Mech. Mater. 148 (2020), 103496.
[36] D.A. García, M.B. Rosales, Deflections in sawn timber beams with stochastic properties, European Journal of Wood and Wood Products 75 (2017) 683–699.
[37] J.B. Berger, H.N.G. Wadley, R.M. McMeeking, Mechanical metamaterials at the theoretical limit of isotropic elastic stiffness, Nature 543 (7646) (2017) 533–537.
[38] P.J. Vrolijk, J.L. Urai, M. Kettermann, Clay smear: review of mechanisms and applications, J. Struct. Geol. 86 (2016) 95–152.
[39] A. Catapano, M. Montemurro, A multi-scale approach for the optimum design of sandwich plates with honeycomb core. Part I: homogenisation of core properties, Compos. Struct. 118 (2014) 664–676.
[40] H. Akoglu, User's guide to correlation coefficients, Turkish journal of emergency medicine 18 (3) (2018) 91–93.
[41] A.G. Asuero, A. Sayago, A.G. González, The correlation coefficient: an overview, Crit. Rev. Anal. Chem. 36 (1) (2006) 41–59.
[42] F.L. Jiménez, N. Triantafyllidis, Buckling of rectangular and hexagonal honeycomb under combined axial compression and transverse shear, Int. J. Solid Struct. 50 (24) (2013) 3934–3946.
[43] S. Novoselac, T. Ergić, P. Baličević, Linear and nonlinear buckling and post buckling analysis of a bar with the influence of imperfections, Teh. Vjesn. 19 (3) (2012) 695–701.
[44] W.S. Lee, M.T. Lin, The effects of strain rate and temperature on the compressive deformation behaviour of Ti-6Al-4V alloy, J. Mater. Process. Technol. 71 (2) (1997) 235–246.
[45] F. Dos Reis, J.F. Ganghoffer, Equivalent mechanical properties of auxetic lattices from discrete homogenization, Comput. Mater. Sci. 51 (1) (2012) 314–321.
[46] F. Djavanroodi, A. Derogar, Experimental and numerical evaluation of forming limit diagram for Ti6Al4V titanium and Al6061-T6 aluminum alloys sheets, Mater. Des. 31 (10) (2010) 4866–4875.
[47] L. Riva, P.S. Ginestra, E. Ceretti, Mechanical characterization and properties of laser-based powder bed–fused lattice structures: a review, Int. J. Adv. Des. Manuf. Technol. 113 (2021) 649–671.
[48] L. Xiao, G. Feng, S. Li, K. Mu, Q. Qin, W. Song, Mechanical characterization of additively manufactured metallic lattice structures with hollow struts under static and dynamic loadings, Int. J. Impact Eng. 169 (2022), 104333.
[49] A. Antolak-Dudka, P. Płatek, T. Durejko, P. Baranowski, J. Małachowski, M. Sarzyński, T. Czujko, Static and dynamic loading behavior of Ti6Al4V honeycomb structures manufactured by Laser Engineered Net Shaping (LENSTM) technology, Materials 12 (8) (2019) 1225.
[50] S.Y. Choy, C.N. Sun, K.F. Leong, J. Wei, Compressive properties of Ti-6Al-4V lattice structures fabricated by selective laser melting: design, orientation, and density, Addit. Manuf. 16 (2017) 213–224.
[51] R. Hussein, S. Anandan, M. Spratt, J.W. Newkirk, K. Chandrashekhara, M. Heath, M. Walker, Effective elastic moduli of metal honeycombs manufactured using selective laser melting, Rapid Prototyp. J. 26 (5) (2020) 971–980.
[52] S.O. Obadimu, K.I. Kourousis, Load-rate effects on the in-plane compressive behaviour of additively manufactured steel 316L honeycomb structures, Eng. Struct. 273 (2022), 115063.
[53] L. Aktay, A.F. Johnson, B.H. Kröplin, Numerical modelling of honeycomb core crush behaviour, Eng. Fract. Mech. 75 (9) (2008) 2616–2630.
[54] A. Chawla, S. Mukherjee, D. Kumar, T. Nakatani, M. Ueno, Prediction of crushing behaviour of honeycomb structures, Int. J. Crashworthiness 8 (3) (2003) 229–235.
[55] M. Stanczak, T. Fras, L. Blanc, P. Pawlowski, A. Rusinek, Numerical modelling of honeycomb structure subjected to blast loading, in: Proceedings of the 12th European LS-DYNA Conf, Koblenz, Germany, 2019, May, pp. 14–16.
[56] Z. Wang, J. Liu, Numerical and theoretical analysis of honeycomb structure filled with circular aluminum tubes subjected to axial compression, Compos. B Eng. 165 (2019) 626–635.
[57] F.L. Jiménez, N. Triantafyllidis, Buckling of rectangular and hexagonal honeycomb under combined axial compression and transverse shear, Int. J. Solid Struct. 50 (24) (2013) 3934–3946.
[58] C. Qiu, Z. Guan, X. Guo, Z. Li, Buckling of honeycomb structures under out-of-plane loads, J. Sandw. Struct. Mater. 22 (3) (2020) 797–821.
[59] R. Guerra Silva, C. Salinas Estay, G. Morales Pavez, J. Zahr Viñuela, M.J. Torres, Influence of geometric and manufacturing parameters on the compressive behavior of 3D printed polymer lattice structures, Materials 14 (6) (2021) 1462.
[60] Y. Liu, X. Liu, C. Lai, J. Ma, X. Meng, L. Zhang, S. Chen, Boriding of tungsten by the powder-pack process: phase formation, growth kinetics and enhanced neutron shielding, Int. J. Refract. Metals Hard Mater. 110 (2023), 106049.
[61] S.H. Pan, G.C. Yao, Y.N. Cui, F.S. Meng, C. Luo, T.Q. Zheng, G. Singh, Additive manufacturing of tungsten, tungsten-based alloys, and tungsten matrix composites, Tungsten 5 (1) (2023) 1–31.
[62] A. Mostafaei, R. Ghiaasiaan, I.T. Ho, S. Strayer, K.C. Chang, N. Shamsaei, A.C. To, Additive Manufacturing of Nickel-based superalloys: a state-of-the-art review on process-structure-defect-property relationship, Prog. Mater. Sci. (2023), 101108.
[63] C.Y. Yap, C.K. Chua, Z.L. Dong, Z.H. Liu, D.Q. Zhang, L.E. Loh, S.L. Sing, Review of selective laser melting: materials and applications, Appl. Phys. Rev. 2 (4) (2015).
[64] F. Careri, R.H. Khan, C. Todd, M.M. Attallah, Additive Manufacturing of Heat Exchangers in Aerospace Applications: A Review, Applied Thermal Engineering, 2023, 121387.
[65] F. Singer, D.C. Deisenroth, D.M. Hymas, M.M. Ohadi, Additively manufactured copper components and composite structures for thermal management applications, in: 2017 16th IEEE Intersociety Conference on Thermal and Thermomechanical Phenomena in Electronic Systems (ITherm), IEEE, 2017, May, pp. 174–183.
[66] J. Banhart, Manufacture, characterisation and application of cellular metals and metal foams, Prog. Mater. Sci. 46 (6) (2001) 559–632.
[67] M.J.R. Asadabadi, M. Sheikholeslami, Impact of utilizing hollow copper circular fins and glass wool insulation on the performance enhancement of pyramid solar still unit: an experimental approach, Sol. Energy 241 (2022) 564–575.